Multi-scale Smoothed Finite Element

Micro-mechanical Material Analysis

Petr Henyš,

2019

Contents

Abstrakt

Simulace v materiálovém inženýrství musí uvažovat složité fyzikální jevy, které mají nelineární charakter a interagují na vícero časových a prostorových měřítkách. I přes bouřlivý vývoj výpočetních technologií, simulace s prostorovým a časovým rozlišením prostupující významně rozdílná měřítka počínaje elektronovou strukturou a konče okem viditelnou jsou i nadále realizovatelné jen velmi omezeně. Tato práce je věnována více-škálové homogenizaci od matematické formulace až po konstrukci modelu odvozeného z reálných dat. V první části je představena nová implementace periodických okrajových podmínek ve smyslu Nitscheho metody a následně otestována na komplexních materiálových strukturách. V druhé části je představena technika vyhlazování gradientu a její využití pro zlepšení konvergenčních vlastností metody konečných prvků a přesnosti odhadu efektivních materiálových vlastností. Třetí část práce je věnována efektivní zpětné rekonstrukci vlákenných textilních struktur z tomografických dat včetně odhadu morfologických parametrů.

Klíčová slova: *periodické okrajové podmínky, metoda konečných prvků, více-škálové modelování, vyhlazení gradientu, Nitscheho metoda, mikro CT, obrazová analýza*

Abstract

Simulations in material engineering must consider complex physical phenomena that have a non-linear character and interact with multiple time and space scales. In spite of the intensive development of computational technologies, spatial and temporal simulations penetrating significantly different scales, starting with the electron structure and visible at the end, can still be realized only very limited. This work is devoted to multi-scale homogenization starting from mathematical formulation and ends up with the construction of a model derived from real data. The first part introduces a new implementation of periodic boundary conditions in the sense of the Nitsche's method and subsequently tested on complex material structures. The second part introduces the gradient smoothing technique and its use to improve the convergence properties of the finite element method and the accuracy of the estimation of the effective material properties. The third part is devoted to the effective reconstruction of fibrous textile structures from tomographic data including the estimation of morphological parameters.

Keywords: *periodic boundary conditions, finite element method, multi-scale modelling, gradient smoothing, Nitsche's method, micro CT, image analysis*

Goals and Contribution

Scales and complex physic drive the scientific community to develop sophisticated and efficient computational methods. Although we see the intensive evolution of computer technologies, using them for a "simple" simulation of tensile response of "simple" beam made of "simple" material is still challenging and many simplified assumptions on physic and geometry must be made before. It is a complexity of real world and our limited understanding whose inspired for developing of the multi-scale approaches. Coupling the different physics and the different temporal or spatial scales are the attractive procedures, but requires infeasible amount of computing/time sources, no even achievable today at many situation. Nevertheless, being so sceptical is not in place and it must be pointed out that the computational multiscaling or homogenisation can help us to reduce significantly the computer sources and still keep the simulations within at least somehow realistic assumptions. The computational homogenisation/multi-scale sometimes called as FE^2 is well established today and provide a powerful framework for simulating the complex non-linear mechanics at several scales. Nevertheless, issues related to accuracy, model preparation and periodicity must be pointed out. The periodicity is often required on the computational model with complex material phases and geometry. This is a serious issue as the given geometry and physic is discretised by finite element method and hence the new formulation of periodicity constraints in Nitsche's sense is proposed in this study. Further, the accuracy of the first order finite element discretisation is often not sufficient as the speed is preferred. Using a gradient smoothed homogenisation (as proposed in this study) leads to better accuracy/convergence while maintaining the efficiency of the first order discretisation. The study provides an intensive numerical benchmarks including complex geometrical models such textile material structures or meta-material structure. At the last chapter, the micro CT-based reconstruction of fibre-like fabric is introduced in order to get complex, real-geometry based computational model for the homogenisation.

The goal of the study is to develop an efficient and accurate homogenization framework including the intensive numerical tests and algorithms for extraction of complex fibre-like structures based on micro CT data. The scientific contribution is highlighted:

- Review of periodicity enforcement on models with non-conformal boundary discretisation.
- Novel periodicity constraints enforcement based on the Nitsche's method

including the estimation of stabilisation parameter and its intensive numerical testing.

- Accuracy and convergence improvement of first order homogenisation method by smoothing the gradient and its extensive testing.
- Novel method for extracting the fibre-like structure from microCT data tested on woven fabric and yarn structures.

Chapter 1

Periodic Boundary Conditions for Computational Homogenization

1.1 Introduction

Computational homogenisation is an effective method for incorporating multi-scale hierarchies into computational models [28]. The simulations of heterogeneous materials and their material properties, which are based on micro-scale data, considerably benefit from computational homogenisation since it can account for complicated and possibly non-linear structural behaviour [70]. The basic idea behind computational homogenisation is to couple two computational models (one micro-scale model and a macro-scale model) by solving an auxiliary micro-scale boundary value problem (BVP) at the macro-scale model's integration points. However, the computational cost of this solution process can be high, meaning that additional work is usually required to find ways of reducing the computational complexity [39, 66]. With computational

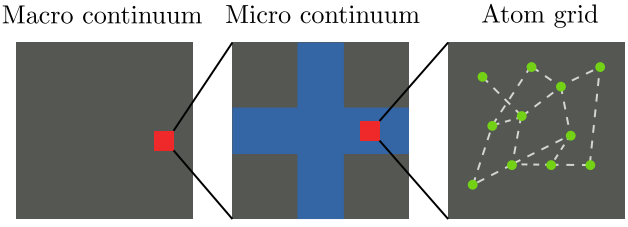

Figure 1.1: A three scale computational model, top-bottom approach-from macro continuum to atomic model

homogenisation, the associated micro-scale model's boundaries need to be de-

fined such that the macro-scale model's behaviour is correctly captured and the Mandel–Hill condition is satisfied [59]. This usually means that either Dirichlet or Neumann boundary condition is applied, but the most important issue in terms of ensuring that the model is accurate and effective is how the boundaries are treated. Traditional uniformly distributed boundary conditions require the micro-scale model to be larger to correctly capture the properties at that scale. While periodic boundary conditions (PBCs) can provide better approximations than uniformly distributed conditions (even for non-periodic geometries), they require additional effort to be put into the meshing procedure and treatment of the underlying mathematical solution [50, 98].

Periodicity constraints require opposite nodes of the representative volume element (RVE) to match, and Lagrange multipliers, penalty methods or direct elimination can be used to impose periodicity. However, when there are pairs of non-conforming opposite nodes (e.g. in non-periodic meshes), substantially more effort is required to handle the periodicity constraint and obtain a reasonable solution. Certainly, not restricting the meshing process offers great flexibility (e.g. homogenisation based on the complex material structures obtained from micro-computed tomography). In the last decade, several approaches for maintaining the periodicity of non-conforming meshes have been proposed.

Tyrus et al. implemented a method that interpolates the periodic constraints piecewise in a way that only affects the corresponding degrees of freedom (DOFs) at the boundaries [100]. This strategy allows the local finite-element matrices to be reformulated, and no additional treatment is required. Later, a natural extension of this method was introduced [74], which avoided the need to know the RVE structure *a priori*. Larsson et al. modelled PBCs weakly within an additional finite element (FE) discretisation process [95]. Another study used a master–slave approach to enforce PBCs [112]. The so-called mortar approach for weakly enforcing the boundary conditions (discussed later in subsection 1.2.2) was investigated in previous research [92]. Ouchetto et al. represented the periodicity conditions in terms of the combined nodal values of opposite faces [80]. A more recent study [104] presented an interesting approach based on the radial interpolation technique commonly used in meshless methods. Finally, Jacques et al. handled non-matching faces using a simple approach, which involved an external grid with local reference points that could possibly be implemented in commercial software [42].

The above literature review indicates that there is still more work to be done on enforcing PBCs on non-matching meshes, even though efficient and accurate implementation is a crucial step for achieving good multi-scale ho-

mogenisation performance. This study compares several methods in terms of accuracy, effectiveness and flexibility. In addition, based on Nitsche's method, we present a new approach that weakly enforces PBCs on non-matching faces and compare it with the current methods [49, 108]. We demonstrate the methods using a linear elastostatic framework using first-order homogenisation to obtain material effective properties and a nested two-scale scheme and later extended to 3D.

1.2 Homogenisation on Non-Periodic Meshes

Our goal is to solve the following linear elasticity problem, with primary variable displacement $\mathbf{u}$ and periodicity/anti-periodicity constraints on the edges.

$$\begin{aligned}
-\nabla \cdot \boldsymbol{\sigma} &= \mathbf{0} && \text{on } \Omega \\
\boldsymbol{\sigma} \cdot \mathbf{n} &= \mathbf{0} && \text{on } \Gamma \\
\mathbf{u}_{\Gamma_{23}} - \mathbf{u}_{\Gamma_{41}} &= \hat{\varepsilon}(x_{\Gamma_{23}} - x_{\Gamma_{41}}) && \text{on } \Gamma_{23} \text{ and } \Gamma_{41} \\
\mathbf{u}_{\Gamma_{34}} - \mathbf{u}_{\Gamma_{12}} &= \hat{\varepsilon}(x_{\Gamma_{34}} - x_{\Gamma_{12}}) && \text{on } \Gamma_{34} \text{ and } \Gamma_{12} \\
\boldsymbol{\sigma}_{\Gamma_{23}} \cdot \mathbf{n}_{\Gamma_{23}} &= -\boldsymbol{\sigma}_{\Gamma_{41}} \cdot \mathbf{n}_{\Gamma_{23}} && \text{on } \Gamma_{23} \\
\boldsymbol{\sigma}_{\Gamma_{34}} \cdot \mathbf{n}_{\Gamma_{34}} &= -\boldsymbol{\sigma}_{\Gamma_{12}} \cdot \mathbf{n}_{\Gamma_{34}} && \text{on } \Gamma_{34}
\end{aligned} \tag{1.1}$$

Here, $\boldsymbol{\sigma}$ is the stress tensor and $\hat{\varepsilon}$ is the macroscopic small-strain tensor evaluated at the macroscopic Gauss integration points $\mathbf{x}^{gp}$. The geometrical domain is a simple square $\Omega \in [\mathrm{l} \times \mathrm{l}]$ with voids/inclusions and outward normals $\mathbf{n}$, as shown in Figure 1.2. The edge and point boundaries are denoted in clockwise order.

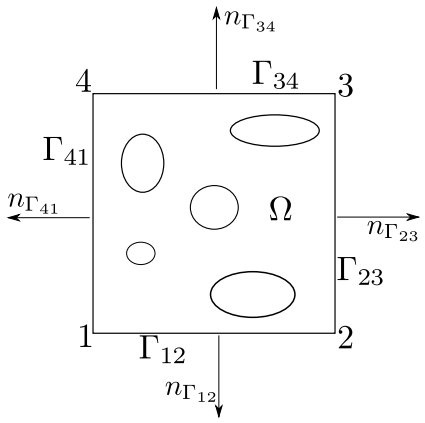

Figure 1.2: Geometrical domain with periodic boundary conditions.

Under the small-strain assumption, the infinitesimal strain tensor $\boldsymbol{\varepsilon}$ is defined as follows:

$$\boldsymbol{\varepsilon} = \frac{1}{2}(\nabla \mathbf{u} + \nabla^T \mathbf{u}). \tag{1.2}$$

The constituent relation for this tensor is expressed as follows:

$$\boldsymbol{\sigma} = \mathbb{C} : \boldsymbol{\varepsilon}, \tag{1.3}$$

where the elasticity tensor $\mathbb{C}$ for the isotropic material can be written as follows:

$$C_{ijkl} = \frac{E\mu}{(1+\mu)(1-2\mu)}\delta_{ik}\delta_{kl} + \frac{E}{1+\mu}\delta_{il}\delta_{jk}. \tag{1.4}$$

The variables E and μ are Young's modulus and Poisson's ratio, respectively, and δ_{ij} is the Kronecker delta.

1.2.1 Homogenisation

The macro-scale quantities $\hat{\boldsymbol{\sigma}}$ and $\hat{\boldsymbol{\varepsilon}}$ are related to their micro-scale counterparts by the average operator as follows:

$$\begin{aligned} \hat{\boldsymbol{\sigma}} &= \frac{1}{\Omega}\int_\Omega \boldsymbol{\sigma}\ \mathrm{d}\Omega, \\ \hat{\boldsymbol{\varepsilon}} &= \frac{1}{\Omega}\int_\Omega \boldsymbol{\varepsilon}\ \mathrm{d}\Omega. \end{aligned} \tag{1.5}$$

The scale transition's consistency is ensured by the Hill–Mandel condition which is expressed as follows:

$$\hat{\boldsymbol{\sigma}} : \hat{\boldsymbol{\varepsilon}} = \frac{1}{\Omega}\int_\Omega \boldsymbol{\sigma} : \boldsymbol{\varepsilon}\ \mathrm{d}\Omega. \tag{1.6}$$

By decomposing the microscopic displacement field $\mathbf{u}$ at the RVE boundary into macroscopic mean and microscopic fluctuations, we obtain the following equation:

$$\mathbf{u}(\hat{x}, x) = \hat{\boldsymbol{\varepsilon}}\hat{x} + \mathbf{u}_m(x). \tag{1.7}$$

Where $\hat{x}, x$ are macroscopic and sub-scale fluctuation coordinates respectively. To ensure that the Hill–Mandel conditions hold for the decomposition in Eq. (1.7), we must impose appropriate boundary conditions. Although the PBCs fulfil these conditions [53], the model is not well posed (the periodicity constraints still allow rigid translational movements), so we need to enforce the following additional integral constraints (for more details, see [74, 75]):

$$\int_\Gamma \mathbf{u}\ \mathrm{d}\Gamma = \mathbf{0}. \tag{1.8}$$

1.2.2 Constraint Treatment

The governing constraints for periodic meshes (Eq. (1.1)) can be efficiently handled by common methods, e.g. direct elimination, penalties and Lagrange approach. However, non-periodic meshes are significantly trickier to deal with. The constraints are essentially continuity-related and can be reformulated as the jump and average operators:

$$[\![\mathbf{u}]\!] = \mathbf{u}_+ - \mathbf{u}_- - \mathbf{g}^0, \tag{1.9}$$

$$\{\boldsymbol{\sigma}\} = \gamma\boldsymbol{\sigma}_+ + (1-\gamma)\boldsymbol{\sigma}_-, \tag{1.10}$$

where we have introduced $\Gamma_{23}\cup\Gamma_{34} \in \Gamma_+$, $\Gamma_{41}\cup\Gamma_{12} \in \Gamma_-$ and $\hat{\varepsilon}(x_+ - x_-) = \mathbf{g}_0$. Furthermore, γ is a parameter of range $0/1/0.5$. The usual average operator is obtained if $\gamma = 0.5$ is set up. Taking $\gamma = 1$ or $\gamma = 0$ results in the one-sided mortar method. To make the formulation consistent, the jump operator includes the macroscopic part of the deformation, but this is then moved to the right-hand side at Eqs. (1.15) and (1.16). There are two possible approaches for dealing with these operators: interpolation (which is meshless) and FE discretisation of the weakly enforced constraints. Both these approaches are discussed below.

Interpolation Method

The interpolation-based methods mainly differ in terms of the type of interpolation scheme used. The simplest scheme uses global Lagrange polynomials and yields surprisingly good results [100, 74]. Although we recommend using more stable polynomials, e.g. Hermite polynomials or B-splines, there are essentially no restrictions on which ones can be selected. The main idea is to express the displacement field $\mathbf{u}$ at the boundaries Γ using the following expansions:

$$\mathbf{u}_-(s) = \sum_{i=1}^{N_n} q_i \mathrm{N}^i(s), \tag{1.11}$$

$$\mathbf{u}_+(s) = \sum_{i=1}^{N_n} q_i \mathrm{N}^i(s) + \mathbf{g}^0. \tag{1.12}$$

Here, N_n is the interpolation order and N^i is the interpolation shape function. Additionally, the unknown coefficient vector $\mathbf{q}$ must be computed. To incorporate these expansions into the FE framework, we can augment the FE matrix (e.g. the stiffness matrix $\mathbf{K}_e$) with the constraint matrix $\mathbf{M}_e$ and

load vector $\mathbf{g}_e^0$ as follows at element level:

$$\Big[\bigcup_{e=1}^{N_e}\mathbf{M}_e^T\mathbf{K}_e\mathbf{M}_e\Big]\begin{Bmatrix}\mathbf{u}\\ \mathbf{q}\end{Bmatrix}=\bigcup_{e=1}^{N_e}\mathbf{M}_e^T(\mathbf{F}_e-\mathbf{K}_e\mathbf{g}_e^0), \tag{1.13}$$

where $\mathbf{F}_e$ represents the original load vector (e.g. volume force) and N_e is the number of elements. The details of how to construct the constraint matrix $\mathbf{M}_e$ and load vector $\mathbf{g}_e^0$ can be found in previous research [100, 75, 74]. The big cup $\bigcup$ represents the assembling operator of FE element matrices. Restriction of the rigid body movement and removing redundant constraints can be made either by Eq. (1.8) or by equating the corner displacement $\mathbf{u}$ to corner coefficients $\mathbf{q}$. This leads to the following relations:

$$\begin{aligned} q_1^x &= u_1 & \qquad q_N^x &= u_4\\ q_1^y &= u_1 & \qquad q_N^y &= u_2 \end{aligned} \tag{1.14}$$

Mortar Discretisation

Mortar discretisation is generally the favoured method and has optimal properties, but it requires us to devise a stable scheme as Lagrange multipliers are the core components of the approach. To enforce continuity, we introduce the idea of mortar and non-mortar edges. Incorporating the jump and average operators defined above leads to the following weak PBC formulation: Find $(\mathbf{u},\boldsymbol{\lambda})\in\mathcal{U}\times\Lambda$ such that

$$\begin{aligned}\int_\Omega\boldsymbol{\varepsilon}(\mathbf{u}):\boldsymbol{\sigma}(\mathbf{v})\,\mathrm{d}\Omega+\int_{\Gamma_+}\{\boldsymbol{\lambda}\}\cdot[\![\mathbf{v}]\!]\,\mathrm{d}\Gamma+\\ \int_{\Gamma_+}\{\mathbf{q}\}\cdot[\![\mathbf{u}]\!]\,\mathrm{d}\Gamma=\int_{\Gamma_+}\{\mathbf{q}\}\cdot\mathbf{g}_0\,\mathrm{d}\Gamma,\end{aligned} \tag{1.15}$$

for all $(\mathbf{v},\mathbf{q})\in\mathcal{V}\times\mathcal{Q}$. The discretisation of the mixed space is P1/P1, as proposed in a previous study [92].

Nitsche's Method

Nitsche's method is a convenient way to weakly enforce constraints without additional DOFs. The Lagrange multipliers are replaced by the boundary flux (in the weak mortar form defined in (1.15)), a penalty term parameterised by β is added to stabilise the solution[1]. Reformulating the PBCs

[1]Depending on whether the symmetrisation terms are included, we can obtain symmetric ($\alpha=1$), asymmetric ($\alpha=0$) and skew-unsymmetric ($\alpha=-1$) formulations.

according to Nitche's method, we obtain the standard form used in the literature [76]:

$$\begin{aligned} \int_{\Omega} \boldsymbol{\varepsilon}(\mathbf{u}) : \boldsymbol{\sigma}(\mathbf{v}) \, \mathrm{d}\Omega - \int_{\Gamma_+} (\llbracket \mathbf{v} \rrbracket \otimes \mathbf{n}) : \{\boldsymbol{\sigma}(\mathbf{u})\} \, \mathrm{d}\Gamma - \\ \alpha \int_{\Gamma_+} (\llbracket \mathbf{u} \rrbracket \otimes \mathbf{n}) : \{\boldsymbol{\sigma}(\mathbf{v})\} \, \mathrm{d}\Gamma + \frac{1}{\beta} \int_{\Gamma_+} \llbracket \mathbf{u} \rrbracket \cdot \llbracket \mathbf{v} \rrbracket \, \mathrm{d}\Gamma = - \\ \alpha \int_{\Gamma_+} \mathbf{g}_0 \cdot (\{\boldsymbol{\sigma}(\mathbf{v})\} \cdot \mathbf{n}) \, \mathrm{d}\Gamma + \frac{1}{\beta} \int_{\Gamma_+} \mathbf{g}_0 \cdot \llbracket \mathbf{v} \rrbracket \, \mathrm{d}\Gamma. \end{aligned} \tag{1.16}$$

1.2.3 Estimating the Stability of Nitsche's form

The estimated stabilisation parameter β must ensure a coercive bilinear form. The final weak form comprises two parts:

$$a(\mathbf{u}, \mathbf{v}) = \underbrace{\hat{a}(\mathbf{u}, \mathbf{v})}_{\text{bulk}} + \underbrace{a^*(\mathbf{u}, \mathbf{v})_+}_{\text{Nitsche}}. \tag{1.17}$$

Supposing the bulk component is coercive and restricts translational rigid movement, we need to estimate the stabilisation parameter β in such a way that there is a problem-dependent constant, c, satisfying

$$a(\mathbf{u}, \mathbf{u}) > \mathrm{c}^2 ||\mathbf{u}||^2. \tag{1.18}$$

Equation (1.16) can be rewritten as follows:

$$a(\mathbf{u}, \mathbf{u}) = \hat{a}(\mathbf{u}, \mathbf{u}) + \frac{1}{\beta} \int_{+} \llbracket \mathbf{u} \rrbracket \cdot \llbracket \mathbf{u} \rrbracket \, \mathrm{d}\Gamma - (1 + \alpha)(\llbracket \mathbf{u} \rrbracket, \bar{\mathbf{t}})_+, \tag{1.19}$$

where $\bar{\mathbf{t}}$ is a boundary flux. By applying Young's inequality, which is expressed as

$$(\mathbf{u}, \mathbf{v}) \leq \frac{1}{2\epsilon} ||\mathbf{u}||^2 + \frac{\epsilon}{2} ||\mathbf{v}||^2, \tag{1.20}$$

we obtain the following inequality:

$$(\llbracket \mathbf{u} \rrbracket, \bar{\mathbf{t}})_+ \leq \frac{1}{2\epsilon} ||\llbracket \mathbf{u} \rrbracket||_+^2 + \frac{\epsilon}{2} ||\bar{\mathbf{t}}||_+^2. \tag{1.21}$$

Here, ϵ is a positive parameter. Combining (1.19) and (1.21) yields the inequality:

$$a(\mathbf{u}, \mathbf{u}) \geq \hat{a}(\mathbf{u}, \mathbf{u}) + \left(\frac{1}{\beta} - \frac{1 + \alpha}{2\epsilon} \right) ||\llbracket \mathbf{u} \rrbracket||_+^2 - \frac{(1 + \alpha)\epsilon}{2} ||\bar{\mathbf{t}}||_+^2. \tag{1.22}$$

Next, the only task that remains is to bound the boundary flux by a mesh-dependent constant, C^2, such that

$$||\bar{\mathbf{t}}||_+^2 \leq C^2 \hat{a}(\mathbf{u}, \mathbf{u}). \tag{1.23}$$

By substituting (1.23) into (1.22), we obtain the final inequality as follows:

$$a(\mathbf{u}, \mathbf{u}) \geq \left(1 - \frac{(1+\alpha)C^2\epsilon}{2}\right)\hat{a}(\mathbf{u}, \mathbf{u}) + \left(\frac{1}{\beta} - \frac{1+\alpha}{2\epsilon}\right)|||[\![\mathbf{u}]\!]|||_+^2. \tag{1.24}$$

This relation must hold for all $\epsilon > 0$, so the three situations in which it holds can be obtained from the following inequalities:

$$1 - \frac{(1+\alpha)C^2\epsilon}{2} \geq 0, \tag{1.25}$$

$$\frac{1}{\beta} - \frac{1+\alpha}{2\epsilon} \geq 0. \tag{1.26}$$

The final inequality (1.24) thus holds in the following three situations.

- $\alpha = 1$. This leads to a symmetric Nitsche variant. By taking $\epsilon < \frac{1}{C^2}$ and hence $\frac{1}{\beta} > C^2$, both inequalities are fulfilled, yielding a unique solution.
- $\alpha = 0$. This leads to an unsymmetric variant. By taking $\epsilon < \frac{2}{C^2}$ and $\frac{1}{\beta} > \frac{C^2}{4}$, both inequalities are fulfilled, yielding a unique solution.
- $\alpha = -1$. This leads to a skew-unsymmetric variant that has a unique solution for $\epsilon > 0$, irrespective of the stabilisation parameter β.

The global stabilisation parameter β can be estimated from the auxiliary generalised eigenvalue problem:

$$\mathbf{H}\mathbf{u} = \lambda \hat{\mathbf{K}}\mathbf{u}, \tag{1.27}$$

where the matrices $\hat{\mathbf{K}}$ and $\mathbf{H}$ are discrete versions of the bulk and average fluxes in (1.23), respectively. The stabilisation parameter β should then be chosen based on the largest eigenvalue λ_{max} [78]. Here, we only consider the symmetric Nitsche variant with a global estimated stabilisation parameter. In order to overcome the limitation of global estimation of stabilisation for multimaterial domain, the approach based on the weighted average flux operator will be applied [4].

1.3 FE Discretisation

Now that as we defined weak PBCs using Nitsche's terms, we can use the Galerkin FE scheme to approximate the solution of Eqs. (1.1). First, we define the test ($\mathcal{U}$) and trial ($\mathcal{V}$) spaces on Ω as follows:

$$\mathcal{U} = \mathbf{u}(x) \in \mathrm{H}^1(\Omega)|_{\mathbf{u}=\mathbf{u}_0 \text{ on } \Gamma_u} \tag{1.28}$$

$$\mathcal{V} = \mathbf{v}(x) \in \mathrm{H}^1(\Omega)|_{\mathbf{v}=\mathbf{0} \text{ on } \Gamma_u} \tag{1.29}$$

Here, H^1 is a usual FE space of piecewise continuous functions. Now, the task is to find $\mathbf{u} \in \mathcal{U}$ for $\forall \mathbf{v} \in \mathcal{V}$. For convenience, we adopt the widely used Voigt notation, which is expressed as follows:

$$\boldsymbol{\varepsilon}_{2\mathrm{D}} = \begin{bmatrix} \varepsilon_{xx} & \varepsilon_{yy} & 2\varepsilon_{xy} \end{bmatrix}^T, \boldsymbol{\varepsilon}_{3\mathrm{D}} = \begin{bmatrix} \varepsilon_{xx} & \varepsilon_{yy} & \varepsilon_{zz} & 2\varepsilon_{yz} & 2\varepsilon_{xz} & 2\varepsilon_{xy} \end{bmatrix}^T \tag{1.30}$$

$$\boldsymbol{\sigma}_{2\mathrm{D}} = \begin{bmatrix} \sigma_{xx} & \sigma_{yy} & \sigma_{xy} \end{bmatrix}^T, \boldsymbol{\sigma}_{3\mathrm{D}} = \begin{bmatrix} \sigma_{xx} & \sigma_{yy} & \sigma_{zz} & \sigma_{yz} & \sigma_{xz} & \sigma_{xy} \end{bmatrix}^T \tag{1.31}$$

$$\mathbf{n}_{2\mathrm{D}} = \begin{bmatrix} n_x & 0 & n_y \\ 0 & n_y & n_x \end{bmatrix}, \mathbf{n}_{3\mathrm{D}} = \begin{bmatrix} n_x & 0 & 0 & 0 & n_z & n_y \\ 0 & n_y & 0 & n_z & 0 & n_x \\ 0 & 0 & n_z & n_y & n_x & 0 \end{bmatrix} \tag{1.32}$$

We use the standard P1 Lagrange shape function space to discretise the displacement field and geometry. The discrete bulk stiffness is as follows:

$$\mathbf{K}_{bulk} = \int_\Omega \mathbf{B}^T \mathbf{C} \mathbf{B} \, \mathrm{d}\Omega, \tag{1.33}$$

where the strain–displacement matrix $\mathbf{B}_e$ at element level is written as follows:

$$\mathbf{B}_e^{2\mathrm{D}} = \begin{bmatrix} \frac{\partial N_1}{\partial x} & 0 & \frac{\partial N_2}{\partial x} & 0 & \cdots \\ 0 & \frac{\partial N_1}{\partial y} & 0 & \frac{\partial N_2}{\partial y} & \cdots \\ \frac{\partial N_1}{\partial y} & \frac{\partial N_1}{\partial x} & \frac{\partial N_2}{\partial y} & \frac{\partial N_2}{\partial x} & \cdots \end{bmatrix} \tag{1.34}$$

$$\mathbf{B}_e^{3\mathrm{D}} = \begin{bmatrix} \frac{\partial N_1}{\partial x} & 0 & 0 & \frac{\partial N_2}{\partial x} & 0 & 0 & \cdots \\ 0 & \frac{\partial N_1}{\partial y} & 0 & 0 & \frac{\partial N_2}{\partial y} & 0 & \cdots \\ 0 & 0 & \frac{\partial N_1}{\partial z} & 0 & 0 & \frac{\partial N_2}{\partial z} & \cdots \\ 0 & \frac{\partial N_1}{\partial z} & \frac{\partial N_1}{\partial y} & 0 & \frac{\partial N_2}{\partial z} & \frac{\partial N_2}{\partial y} & \cdots \\ \frac{\partial N_1}{\partial z} & 0 & \frac{\partial N_1}{\partial x} & \frac{\partial N_2}{\partial z} & 0 & \frac{\partial N_2}{\partial x} & \cdots \\ \frac{\partial N_1}{\partial y} & \frac{\partial N_1}{\partial x} & 0 & \frac{\partial N_2}{\partial y} & \frac{\partial N_2}{\partial x} & 0 & \cdots \end{bmatrix}$$

where N_i is i$^{\text{th}}$ shape function associated with element e. The size of $\mathbf{N}_e, \mathbf{B}_e$ depends on the type of element and the space dimension. The matrix $\mathbf{C}$ is

an elasticity matrix for a linear isotropic material (under the plane stress assumption), which is defined according to (1.4) and represented using Voigt notation. For the other terms, the jump and average operators are as follows:

$$[\![\mathbf{u}]\!] = \mathbf{N}^+\bar{\mathbf{u}}_+ - \mathbf{N}^-\bar{\mathbf{u}}_-, \tag{1.35}$$
$$[\![\mathbf{v}]\!] = \mathbf{N}^+\bar{\mathbf{v}}_+ - \mathbf{N}^-\bar{\mathbf{v}}_-, \tag{1.36}$$
$$\{\boldsymbol{\sigma}(\mathbf{u})\} = \gamma\mathbf{C}^+\mathbf{B}^+\bar{\mathbf{u}}_+ + (1-\gamma)\mathbf{C}^-\mathbf{B}^-\bar{\mathbf{u}}_-, \tag{1.37}$$
$$\{\boldsymbol{\sigma}(\mathbf{v})\} = \gamma\mathbf{C}^+\mathbf{B}^+\bar{\mathbf{v}}_+ + (1-\gamma)\mathbf{C}^-\mathbf{B}^-\bar{\mathbf{v}}_-. \tag{1.38}$$

Here, the matrices $\mathbf{N}_e^+$ and $\mathbf{N}_e^-$ at element level have the arbitrary structure:

$$\mathbf{N}_e = \begin{bmatrix} N_1 & 0 & N_2 & 0 & \cdots \\ 0 & N_1 & 0 & N_2 & \cdots \end{bmatrix}_{\text{2D}}, \mathbf{N}_e = \begin{bmatrix} N_1 & 0 & 0 & N_2 & 0 & 0 & \cdots \\ 0 & N_1 & 0 & 0 & N_2 & 0 & \cdots \\ 0 & 0 & N_1 & 0 & 0 & N_2 & \cdots \end{bmatrix}_{\text{3D}}. \tag{1.39}$$

The vectors $\bar{\mathbf{u}}$ and $\bar{\mathbf{v}}$ represent the trial and test nodal unknowns, respectively. By substituting the discretisations (1.32), (1.34), (1.39) and (1.35) into (1.16) and grouping the terms, we obtain the final matrix form of the scheme:

$$\left[\mathbf{K}_{\text{bulk}} - \mathbf{K}_{\text{Nitsche}} - \alpha\mathbf{K}_{\text{Nitsche}}^T + \frac{1}{\beta}\mathbf{K}_{\text{penalty}}\right]\bar{\mathbf{u}} = -\alpha\mathbf{G}_{\text{Nitsche}} + \frac{1}{\beta}\mathbf{G}_{\text{penalty}}, \tag{1.40}$$

where the vector $\mathbf{G}$ represents load given by $\mathbf{g}^0$ and $\bar{\mathbf{u}}$ the global vector of unknown displacement. The bulk stiffness $\mathbf{K}_{bulk}$ is further decomposed to original problem stiffness $\mathbf{K}_{orig}$ and contribution of constrain integral of Eq. (1.8) $\mathbf{K}_{rmr}$.

1.4 Computational Framework and Solvers

The positive indefinite system is obtained upon the Lagrange multiplier's are present and thus the direct solver MUMPS was used [2]. Handling constraints by the penalty or Nitsche's methods leads to symmetric positive definite system that was used by conjugate gradient method preconditioned by algebraic multigrid HYPRE [19]. The linear algebra and framework is based on the Scipy/PETSc libraries [45, 5]. The generalized eigenvalue problem defined in Eq. (1.27) was solved by the LOBPCG methods [38, 56]. The coding language is the Python/C with parallelisation library MPI [30].

1.5 Integration on Non-Matching Meshes

The main difficulties for both Nitsche's and mortar methods arise as a result of performing integration on non-matching meshes. The most common approaches are the segment- and element-based methods. The idea behind the segment-based method is to introduce an intermediate integration line (surface) on which we integrate the interface fields, as shown in Figure 1.3. The segmentation process requires a computationally demanding procedure

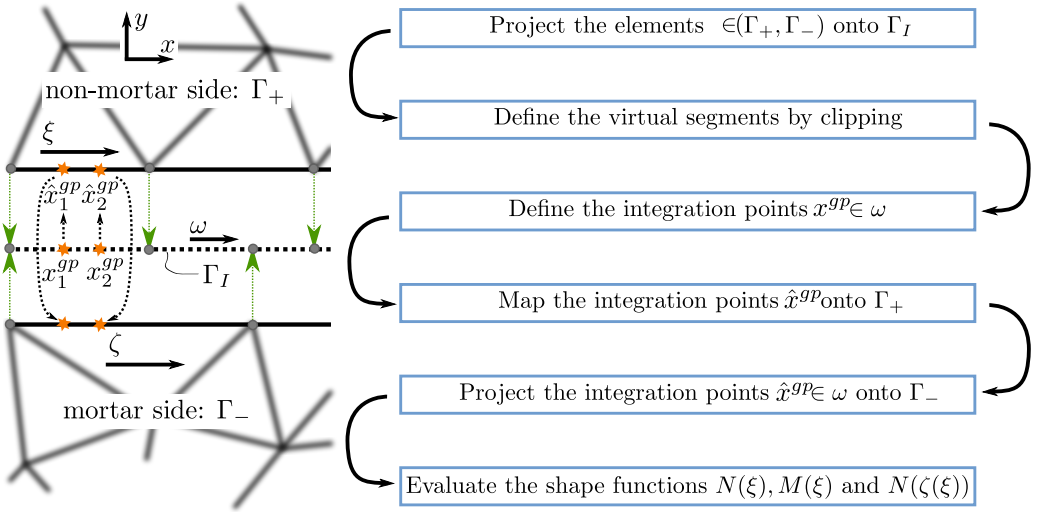

Figure 1.3: Example intermediate mortar surface with two Gauss integration points projected onto the non-mortar/mortar elements. The shape functions $\mathbf{M}(\xi)$ are associated with Lagrange's multipliers on the non-mortar side. Details of the method used to build the virtual segments Γ_I are given in 1.6.

(mainly in 3D) comprising point projection, search and clipping algorithms. In contrast, the element-based method only requires the integration points to be projected onto the non-mortar side. These two approaches are comprehensively compared in previous research [20]. After constructing the virtual segments, it is useful to introduce the segment coordinate system $\omega \in [-1, 1]$ and map the integration points into a coordinate system ξ.

1.6 Projection Strategy for Creating the Virtual Integration Surface

Since the vertex-wise normals for the linear geometry approximation are not unique, we must make some type of approximation to compute unique nor-

mals. One approach is to simply average adjacent values (after first ensuring the cell-wise normals are consistent), as follows:

$$\mathbf{n}_n = \frac{\sum_{e=1}^{N_{adj.}} \mathbf{n}_n^e}{\left\| \sum_{e=1}^{N_{adj.}} \mathbf{n}_n^e \right\|}, \tag{1.41}$$

where $N_{adj.}$ is the number of adjacent cells. The projection method used in this study is based on an idea proposed in [109] and the JuliaFEM FE method package[2]. This strategy is based on setting up the continuous normal field in such a way that the following holds:

$$\left[N_1(\zeta)\mathbf{x}_m^1 + N_2(\zeta)\mathbf{x}_m^2\right] \times \mathbf{n}_{nm} = \mathbf{0}, \tag{1.42}$$

$$\left[N_1(\xi)\mathbf{x}_{nm}^1 + N_2(\xi)\mathbf{x}_{nm}^2 - \mathbf{x}_m\right] \times \left[N_1(\xi)\mathbf{n}_{nm}^1 + N_2(\xi)\mathbf{n}_{nm}^2\right] = \mathbf{0}, \tag{1.43}$$

where the first equation must be solved to project the points on the non-mortar cell defined by the normals $\mathbf{n}_{nm}$ onto the mortar sides defined by the vertices $\mathbf{x}_m$. The latter equation projects each point $\mathbf{x}_m$ on the mortar cell onto the non-mortar cell defined by the vertex-wise normals $\mathbf{n}_s^1$ and $\mathbf{n}_s^2$ and the vertices $\mathbf{x}_{nm}^1$ and $\mathbf{x}_{nm}^2$. This equation is generally non-linear ($\mathbf{n}_s^1 \neq \mathbf{n}_s^2$), except in the case of straight edges (RVEs with no holes that intersect their boundaries).

1.7 Integration of Gradient Operator on Manifold with Double Coordinate Mapping

To evaluate Nitsche's terms in the weak form (1.16), one must make additional effort to properly formulate the gradient operators defined on manifold as the transformation matrix is not squared [14, 47, 85]. Having the local orthonormal(possibly curvilinear) coordinate systems ξ, one can transform covariant components of the gradient operator ∇ to contravariant ones in local system. Having covariant base, defined as the isoparametric transform:

$$\mathrm{a}_{ij} = \sum_{n=1}^{N} \frac{\partial \mathrm{N}_n}{\partial \mathrm{X}^j} x_n^i \ , j < i \tag{1.44}$$

where X^j is the j^{th} component of local coordinate system ξ and the x_n^i is i^{th} coordinate component of m^{th} vertex. From the covariant base can be defined the covariant metric tensor in usual manner

$$\mathbf{h} = \mathbf{a}^T\mathbf{a} \tag{1.45}$$

[2] `www.juliafem.org`

The gradient operator in global coordinate system is formulated with contravariant metric tensor:

$$\bar{\nabla} = \mathbf{h}^{-1}\nabla \tag{1.46}$$

Following the Voigt notation, the matrix of differential operators with contravariant components is defined by contravariant gradient:

$$\bar{\mathrm{B}}^T = \bar{\nabla}\mathbf{N}^T = \mathbf{a}\mathbf{h}^{-1}\nabla\mathbf{N}^T \tag{1.47}$$

$$\mathrm{d}\bar{\Omega} = \sqrt{\det(\mathbf{h})}\ \mathrm{d}\Omega \tag{1.48}$$

In this case the double transformation x $\leftarrow \xi \leftarrow \omega$ of gradient operator has the following structure:

$$\bar{\nabla} = \mathbf{\Delta x}\frac{4}{l_x^2}\Delta\xi\frac{1}{2l_\xi^2}\partial_\omega \tag{1.49}$$

where the $\mathbf{\Delta x}, \Delta\xi$ are the coordinate differences, the l_x, l_ξ are the lengths of the non-mortar cell and virtual segment respectively. The matrix $\mathbf{B}$ has the following structure:

$$\mathbf{B} = \bar{\nabla}\mathbf{N}^T = \frac{2}{l_x^2 l_\xi}\begin{bmatrix} -\Delta x & 0 & \Delta x & 0 \\ 0 & -\Delta y & 0 & \Delta y \\ -\Delta y & -\Delta x & \Delta y & \Delta x \end{bmatrix} \tag{1.50}$$

and differential line:

$$\mathrm{d}\bar{\Omega} = \frac{1}{4}l_x l_\xi \tag{1.51}$$

The usual way is to introduce extra coordinate mapping according to Figure 1.4. The mapping T_i must be linked to proper element's edge and then the edge Gauss points can be mapped onto reference triangle. Using global position of the gauss point X_{gp} one can avoid the extra maps and rather directly remap the gauss point onto local coordinate system of the triangle. The following non-linear equations in a residual form need to be solved:

$$\mathbf{R}(\mathbf{x}, \xi, ...) = \mathbf{X}\mathbf{N}(\xi, ...) - X_{gp} = \mathbf{0} \tag{1.52}$$

where $\mathbf{x}, \xi, ...$ are nodal coordinates and local coordinate system of an element respectively. Further, $\mathbf{X}, \mathbf{N}(\xi, ...)$ are a matrix of coordinates $\mathbf{x}$ and interpolations functions associated with an element. To solve the system of above equations, simple Newton-Rhapson scheme could be used. The analytical Jacobi matrix needed in the iteration scheme can be derived straightforwardly from 1.44. Initial estimate can be placed into barycentric of the element

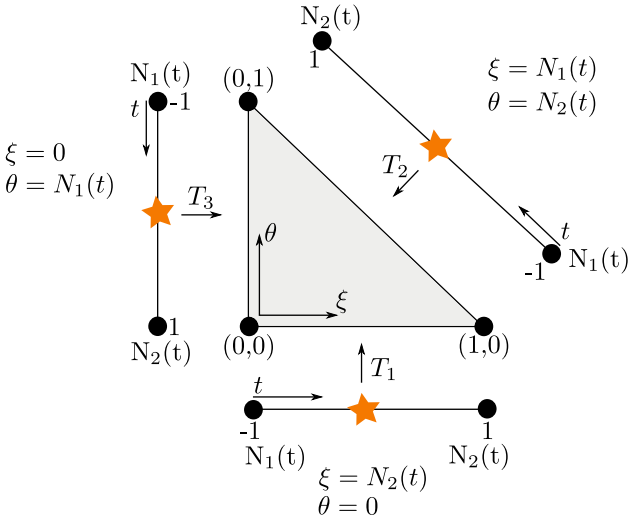

Figure 1.4: Integration on element edges by introducing the extra mapping $\mathrm{T_i} : [-1, 1] \rightarrow \partial\Gamma_i,\ i = 1, 2, 3$. The orange stars are integration points on reference edge.

$\xi, ... = \{\frac{1}{3}, ...\}$ can be used to get the scheme converged after one two iterations to get local coordinates $\xi, ...$ Although the scheme works well and quickly goes to results, it is quite expensive as it needs solving the linear system at least once on many element.

The proposed formulation based on the covariant/contravariant transforms offers a consistent way to treat complicated boundary integrals as well as interior integrals for Nitsche's forms (particular discontinuous Galerkin). The 3D formulation is shown in Figure 1.5. It is a natural generalization of 2D case except the second coordinate transform, which is straightforward and will not be discussed further. Again, computing non-squared Jacobian matrix $\mathbf{J}_g$ of the mapping $\mathrm{x} \leftarrow \xi$ is given by set of linear parametrization functions $\mathbf{N}$ and number m of local coordinate derivatives in 3D at nodal points $\mathbf{x}$:

$$\mathbf{J}_g^{n\times m} = \underbrace{\begin{bmatrix} x_1 & y_1 & z_1 \\ x_2 & y_2 & z_2 \\ x_3 & y_3 & z_3 \\ x_4 & y_4 & z_4 \end{bmatrix}^T}_{\mathbf{x}^T} \underbrace{\begin{bmatrix} -1 & -1 & -1 & -1 \\ 0 & 1 & 0 & 0 \\ 0 & 0 & 1 & 0 \\ 0 & 0 & 0 & 1 \end{bmatrix}}_{\nabla\mathbf{N}\ for\ T3} = \underbrace{\begin{bmatrix} \Delta x_{21} & \Delta x_{31} \\ \Delta y_{21} & \Delta y_{31} \\ \Delta z_{21} & \Delta z_{31} \end{bmatrix}}_{T3} \tag{1.53}$$

Keeping in mind the generalization of covariant metric tensor $\mathbf{h}$ from Eq. (1.45), we obtain:

$$\mathbf{h} = \mathbf{J}_g^T \mathbf{J}_g \tag{1.54}$$

The gradient with respect to global coordinates can be expressed as:

$$\bar{\nabla}\mathbf{N} = \nabla\mathbf{N}\mathbf{h}^{-1}\mathbf{J}_g^T \tag{1.55}$$

The differential is expressed according to expression (1.48). A generalization and prove of the validity of transformation the differential volume on hypersurface / hypervolume are given in [48].

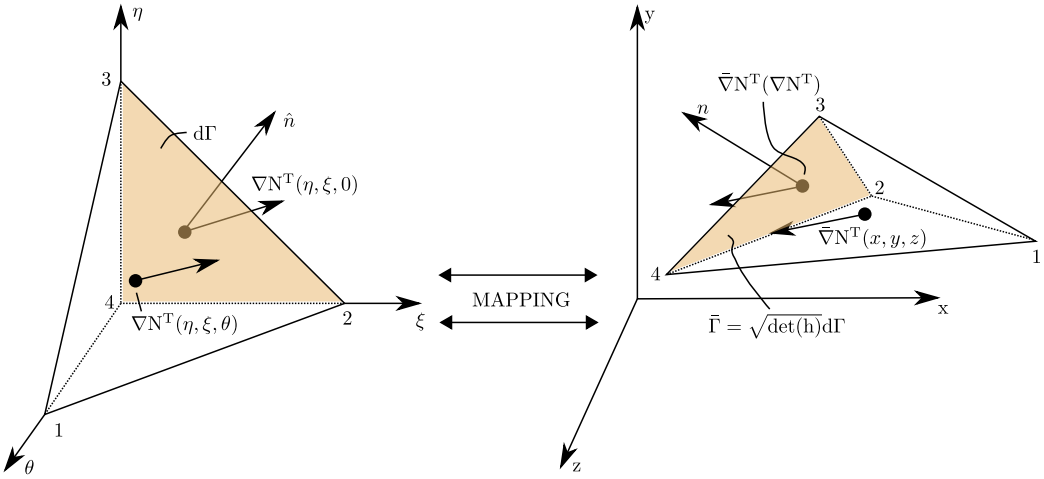

Figure 1.5: Evaluation of gradients on 2D manifold represented as finite element tetrahedral simplex immersed in 3D.

1.8 Numerical Benchmarks 2D

1.8.1 General Setup

The methods discussed in Section 1.2.2 were tested using several benchmarks that focused on robustness, accuracy and efficiency. For the interpolation method, we used Hermite polynomials with 3–10 segments. For the mortar and Nitsche methods, we used the formulation described above by integrating the virtual segments at three Gauss integration points $x^{gp} = \{-\sqrt{\frac{3}{5}}, 0, \sqrt{\frac{3}{5}}\}$ with corresponding weights $w^{gp} = \{\frac{5}{9}, \frac{8}{9}, \frac{5}{9}\}$. The number of integration points at the interface is the same for both mortar and Nitsche methods. Due to material discontinuities, higher number of integration points is somehow needed (especially for mortar method) to get sufficient accuracy of integration scheme. This observation is obtained from extensive numerical tests and is consistent with findings in [20]. The rigid translational constraints (1.8) were

addressed via the penalty method. The Nitsche's term stabilisation penalty parameter was derived locally according to [4] for multi-material RVE[3], or globally with respect to single material RVE [78]. The symmetric variant of Nitsche's method was considered at all examples. The penalty parameter value for (1.8) was in the range 1–100 estimated by means of the extensive numerical tests for RVE employed in this study. The mortar method was taken as a reference method because it has been proven to achieve optimal convergence properties [88, 89, 22, 90, 9, 54, 86, 107, 87] and has been successfully used in homogenization framework [92]. The homogenized elasticity tensor was computed from the response of RVE for unitary fundamental loads defined by macro strains in 2D:

$$\hat{\boldsymbol{\varepsilon}}^{11} = \begin{bmatrix} 1 & 0 \\ 0 & 0 \end{bmatrix}, \hat{\boldsymbol{\varepsilon}}^{22} = \begin{bmatrix} 0 & 0 \\ 0 & 1 \end{bmatrix} \; and \; \hat{\boldsymbol{\varepsilon}}^{12} = \begin{bmatrix} 0 & 0.5 \\ 0.5 & 0 \end{bmatrix}, \tag{1.56}$$

The homogenized elasticity constants were computed as:

$$\hat{\mathrm{C}}_{ijkl} = \frac{1}{V} \int_{\Omega} \varepsilon^{ij}_{mn} \mathrm{C}_{mnop} \varepsilon^{kl}_{op} \, \mathrm{d}\Omega \tag{1.57}$$

where Ω is the domain of RVE with area/volume V and $\varepsilon^{ij}_{mn}, \varepsilon^{kl}_{op}$ are fundamental load combinations [40, 72].

1.8.2 Convergence Analysis of Nitsche's Method

The Nitsche's method convergence behaviour was tested using a squared RVE, $\Omega \in [\mathrm{l_{ref}} \times \mathrm{l_{ref}}]$ mm, containing a circular hole of radius $\mathrm{r} = 0.35$ mm at the centre. The material constituting the RVE were described by their Young's moduli, namely $\mathrm{E} = 1$ GPa and Poisson's ratio of 0.3. The homogenized shear stress was used as an equivalent measure of the H^1 convergence ,which is arbitrary defined as a semi-norm:

$$|\cdot|^2_{H^1(\Omega)} = \int_{\Omega} |(\cdot)'|^2 \, \mathrm{d}\Omega \tag{1.58}$$

and allows us to analyse the convergence of a stress quantity at a given FE space. We calculated the error e by comparing the results with a reference solution obtained using the mortar method:

$$e = \frac{|\hat{\sigma}^{\mathrm{ref}}_{xy} - \hat{\sigma}_{xy}|}{|\hat{\sigma}^{\mathrm{ref}}_{xy}|}. \tag{1.59}$$

[3]Well known global estimation based on the maximal eigenvalue is not suitable for multi phase material model.

To demonstrate the convergence of solution, the micro-model was loaded according to the macro-strain defined as a simple shear load:

$$\hat{\boldsymbol{\varepsilon}} = \begin{bmatrix} 0.00 & 0.01 \\ 0.01 & 0.00 \end{bmatrix}.$$

Further, the jump operator $[\![\cdot]\!]$ was analysed in the L^2 norm:

$$|| \cdot ||^2_{L^2(\Omega)} = \int_\Omega (\cdot)^2 \, \mathrm{d}\Omega \tag{1.60}$$

in order to check the convergence of the jump operator within mesh refinement and for different values of stabilisation parameter β.

1.8.3 Size Convergence of Homogenized Properties

The size effect on the homogenized elasticity was investigated on a two phase composite RVE in 2D with reference size $\Omega \in [\mathrm{l_{ref}} \times \mathrm{l_{ref}}]$ mm (Figure 1.6). The materials constituting the RVE were described by their Young's moduli, namely $\mathrm{E_{inclusion}} = 100$ GPa and $\mathrm{E_{matrix}} = 10$ GPa, with a Poisson ratio of 0.3 in both cases.

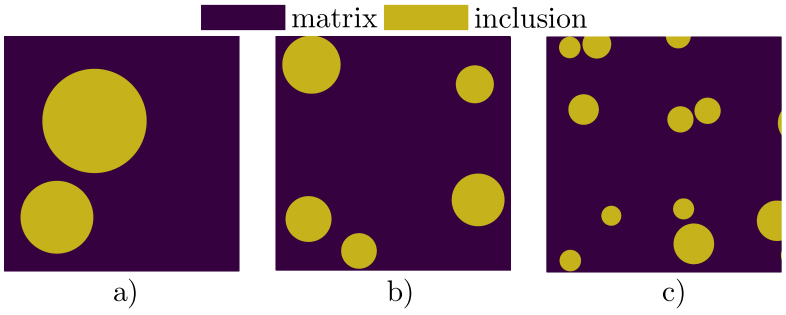

Figure 1.6: Examples of three of the eleven particle scales used for the RVEs: a)$\frac{l}{l_{ref}} = 1$, b)$\frac{l}{l_{ref}} = 2$ and c)$\frac{l}{l_{ref}} = 3$. The particle distribution was generated according to [15].

1.8.4 Two-Scale Beam Analysis

We also evaluated the methods' performance on another test case, namely a loaded beam made from materials with both macro- and micro-scale properties, as shown in Figure 1.7. We used a parallel FE^2 approach based on a scheme proposed in previous research [52, 53]. This test focused on the pro-

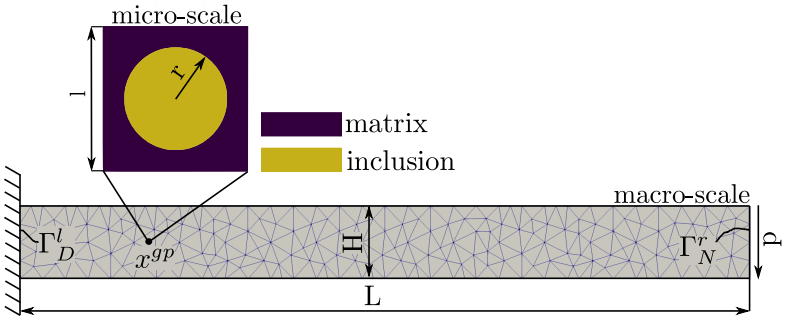

Figure 1.7: Loaded beam fixed at the left edge ($\mathbf{u}_0 = \mathbf{0}$ [mm] $\in \Gamma_{\mathrm{D}}^{\mathrm{l}}$) and loaded by a traction pressure $\mathrm{p} = 0.1\ [\frac{\mathrm{N}}{\mathrm{mm}}] \in \Gamma_{\mathrm{N}}^{\mathrm{r}}$. Here, $\frac{\mathrm{L}}{\mathrm{l_{ref}}} = 1000$ and $\frac{\mathrm{H}}{\mathrm{l_{ref}}} = 100$. The macro-mesh and RVE-mesh sizes are $\frac{\mathrm{H}}{25}$ and $\frac{\mathrm{l_{ref}}}{100}$, respectively.

posed method's overall accuracy and efficiency and used the nested iteration scheme shown in Figure 1.8. The solution was considered to have converged when the norm of residual force $\mathbf{\Delta r}$ was less than 1^{-3}:

$$\mathbf{\Delta r} = \bigcup_{e=1}^{N_e} \mathbf{B}^T \boldsymbol{\sigma}_e \, \mathrm{d}\Omega - \bigcup_{e=1}^{N_e^{\partial}} f_e \, \mathrm{d}\Omega_{\partial}. \tag{1.61}$$

The tangent (macro-elasticity matrix $\mathbf{C}$) was computed by efficiently combining matrix factorisation and a complex-step derivative in a parallel frame [51]:

$$\mathbf{C} = \frac{\partial \hat{\boldsymbol{\sigma}}}{\partial \hat{\boldsymbol{\varepsilon}}}. \tag{1.62}$$

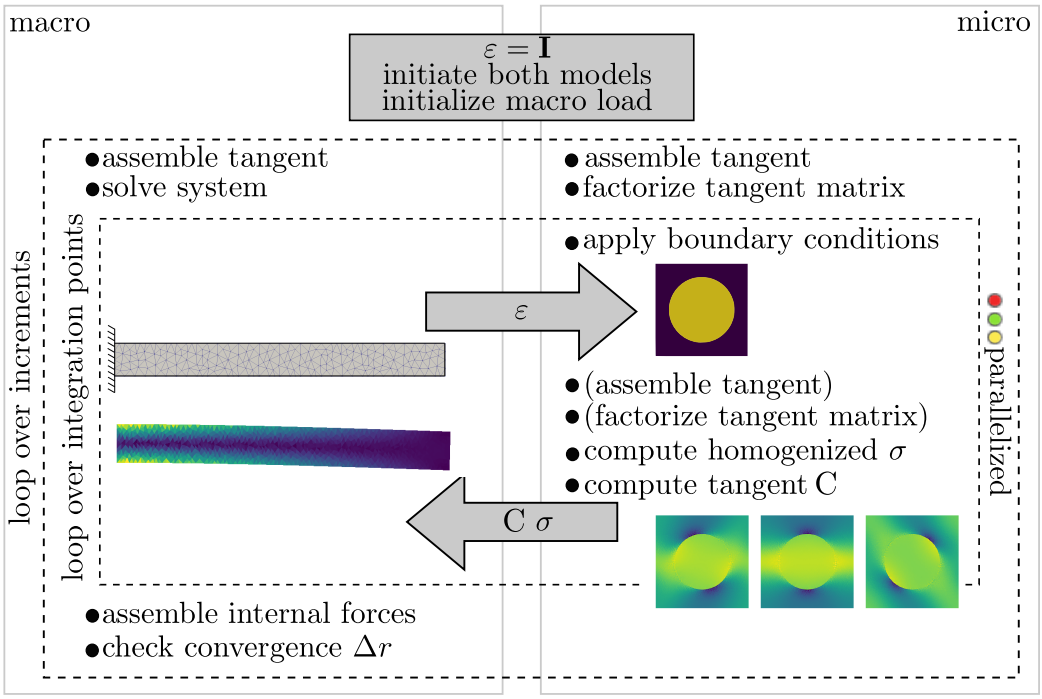

Figure 1.8: Nested iteration scheme used for the two-scale homogenisation analysis. When the RVE geometry and material distribution are constant over the macro-model (micro-periodicity), the efficient factorisation is used. Otherwise, the full-model RVE is generated and solved.

1.8.5 Extension to 3D Analysis

The two dimensional formulation can be, without excessive reformulation, be arbitrarily extended to 3D dimensional space. The integration on non-matching is slightly different from the 2D scheme and hence is shown in Figure 1.9. The clipping algorithm returns a triangulated clipped area based on its centroid. The pre-search algorithm is applied first. The mortar elements' centroids are partitioned by hyper-spheres to get the potential neighbourhoods quickly [79]. Further, the set of potentially intersecting mortar elements is found for an actual non-mortar element by looking at the neighbourhoods in a radius r, which was usually three to five multiple of element's circumradius. In a next step, the mortar elements in the pairing set are tested for the intersection with actual non-mortar element. The 3D periodicity constraints in this study are enforced on the coincident surfaces and hence the virtual interface plane I can be defined on both mortar/non-mortar sides. In this study, the non-mortar element's vertices are projected to mortar element (the projection is associated with a pair of parameters c_{nm}, n_{nm}, which represents the non-mortar centroid and outer normal, respectively). The potential intersection is evaluated by a clipping algorithm [23]. If the number N of shared vertices is > 2 and the clipped area A is non-zero, the newly created polygon is triangulated. In this study a simple triangulation constructed by creating the i^{th} sub-triangle Ω_i along the polygon centroid x_c [92, 20]. In the next step, Gauss-Radau integration points defined by quadrature coordinates and associated weights $\mathbf{x}^{gp}, \mathbf{w}^{gp}$ are generated for each sub-triangle. The integration points are subsequently mapped back into a parametrized domain of non-mortar and mortars elements. The contribution from each polygonal intersection is a sum over the sub-triangles. Surface interpolation based on the Coon patch was employed so as to maintain periodicity in the case of the interpolation method [74]. Gradient needed for Nitche's term is evaluated in the same manner as for 2D within Gauss-Radau integration points for triangular elements. Surface interpolation based on the B-spline tensor product was used to maintain the periodicity in case of interpolation method. In order to test the mentioned methods on a complex geometrical characteristics, three RVEs based on the:

- Poly-crystal grain Structure - **RVE3D-CR**
- Composite with randomly seed inclusions - **RVE3D-I**
- Two phase composite-based meta-material unit - **RVE3D-META**
- Geometrically ideal woven fabric unit - **RVE3D-TEX**

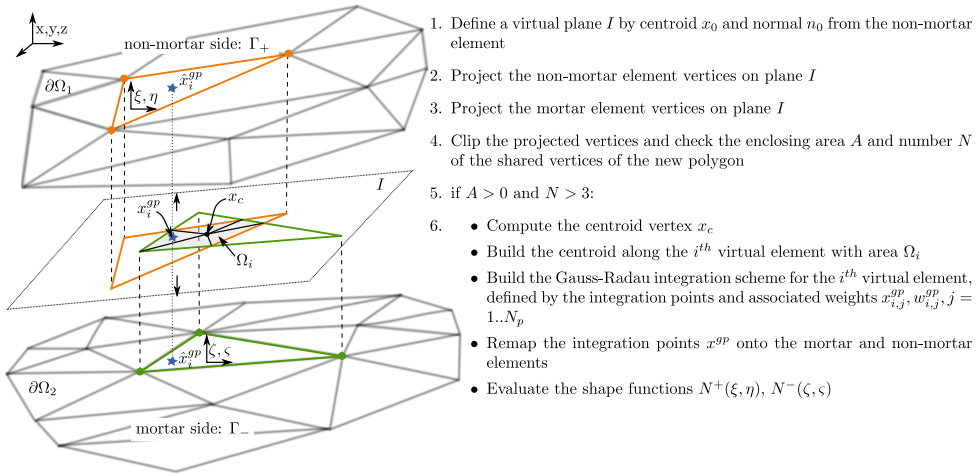

Figure 1.9: Integration on 3D non-conforming mesh boundaries

A linear elastic material model was used as given by one or more material phases. Although the linear approximation of the interface was applied, a greater number of integration points is usually required so as to obtain sufficient precision due to the material discontinuities; hence, the 5-point Gauss integration rule was employed in this sub-study to get accurate integral evaluation [20].The homogenized elasticity tensor was obtained by solving the RVE equilibrium for six fundamental unitary load cases:

$$\hat{\boldsymbol{\varepsilon}}^{11} = \begin{bmatrix} 1 & 0 & 0 \\ 0 & 0 & 0 \\ 0 & 0 & 0 \end{bmatrix}, \hat{\boldsymbol{\varepsilon}}^{22} = \begin{bmatrix} 0 & 0 & 0 \\ 0 & 1 & 0 \\ 0 & 0 & 0 \end{bmatrix} \hat{\boldsymbol{\varepsilon}}^{33} = \begin{bmatrix} 0 & 0 & 0 \\ 0 & 0 & 0 \\ 0 & 0 & 1 \end{bmatrix}, \tag{1.63}$$

$$\hat{\boldsymbol{\varepsilon}}^{23} = \begin{bmatrix} 0 & 0 & 0 \\ 0 & 0 & 0.5 \\ 0 & 0.5 & 0 \end{bmatrix}, \hat{\boldsymbol{\varepsilon}}^{13} = \begin{bmatrix} 0 & 0 & 0.5 \\ 0 & 0 & 0 \\ 0.5 & 0 & 0 \end{bmatrix} \hat{\boldsymbol{\varepsilon}}^{12} = \begin{bmatrix} 0 & 0.5 & 0 \\ 0.5 & 0 & 0 \\ 0 & 0 & 0 \end{bmatrix}. \tag{1.64}$$

The coefficients of homogenized elasticity tensor were computed according (1.57).

Small Deformation of Grain-like Structure

The Figure 1.10 shows a typical RVE used for simulating of crystal plasticity consisting in grains of material phases. The geometrical characteristic is unique, as there are many crystals with different volumes. It is an important task, where the homogenization constraint plays important role and thus it is included in a simplified form in benchmark. In this sub-study, only the geometry is used and the linear elastic properties are computed, although

the crystal plasticity is highly important topic in computational material engineering, but it is over the scope of this study. The grain-like structure was generated on the RVE unit of characteristic length $[1 \times 1 \times 1]$ mm. The RVE contains 250 grain cells with mesh resolution 0.05 and isotropically oriented. The grain size is sampled from uniform distribution as the material properties. The grain interface is expected to be ideal and infinitely stiff.

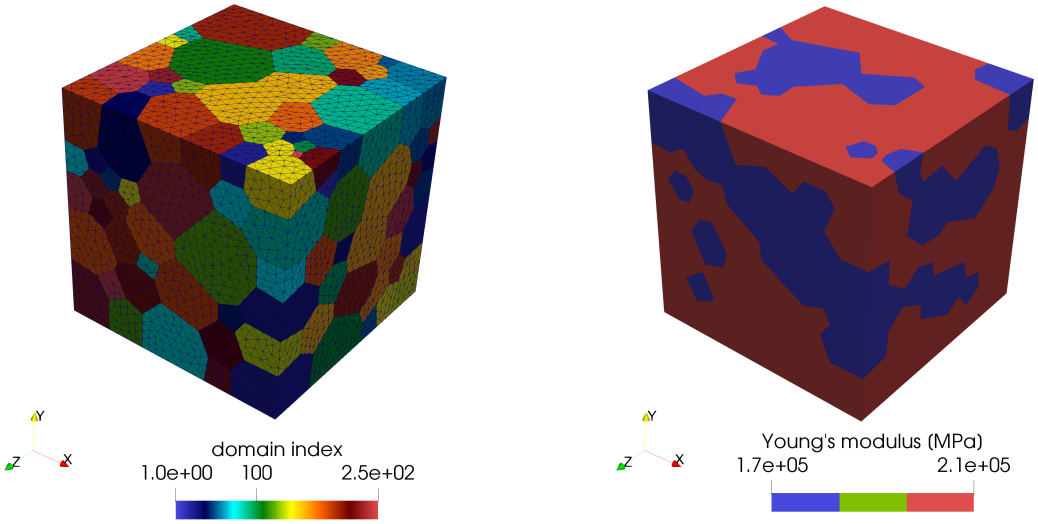

Figure 1.10: The snapshot of crystal model; left-computational mesh and domain index of each crystal, right: two phases(austenitic(blue), ferritic(red). The distribution of characteristic grain size is normal $\mathcal{N}(0.15, 0.01)$ for both phases. The model was generated by by library Neper 3.0 [91].

Soft particle-matrix Composite

The particle composite RVE shown in Figure 1.11 has a dimension 1x1x1 mm with hard spherical inclusions of defined size/position distribution with small overlaps defined as 10% of characteristic particle distance (see details in library Mote3D [94]). Each composite phase is defined by Young's modulus (Figure 1.11:left) and Poisson's ratio, which is same for both phases and has value 0.3.

Two Phase soft Metamaterial

The state-of-the-art so-called "soft" composite with soft matrix and hard auxetic structure is shown in Figure 1.12. Metamaterials have unusual mechanical properties hardly seen in nature. The auxetic structures is famous

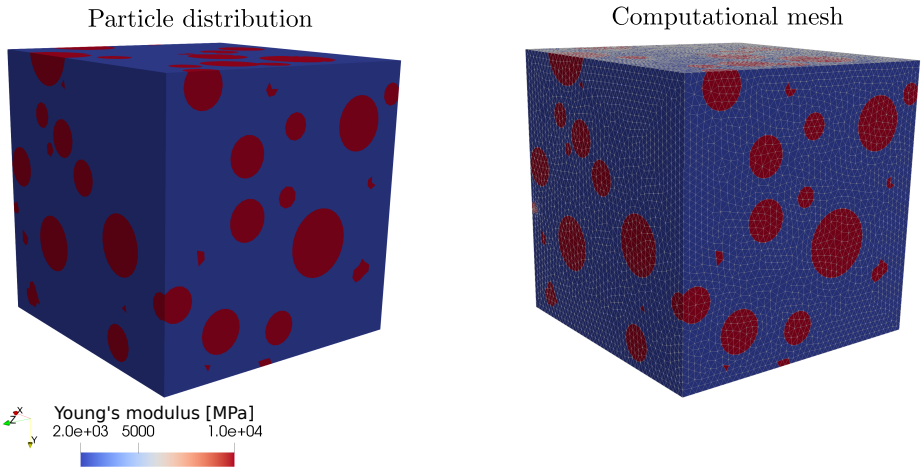

Figure 1.11: The RVE of particle composite with normal distribution defined by $\mathcal{N}(0.1, 0.03)$ of particle radius. The targeted number of particles is 250, but it varies from 245 - 251 per realization. The particle positions and radius are generated in library Mote3D [94].

for its negative Poisson's ratio and increased shear capacity. Adding more material phases together is highly promising area of composites structure engineering (see some last recent results in [58, 43]). This sub-study test very base soft composite with reentrant structure. Poisson's ratio and normal/shear modules are studied in sense of different periodic boundary conditions implementation. The geometrical structure has a dimension $[1 \times 1 \times 0.5]$ mm. The thickness of wall is 0.3 mm and reentrant angle 74°.

Woven Textile Composite

The textile composite cell is defined by woven fabric with three layers with simple structure shown in Figure 1.13. The yarn length is 1 mm with height 0.25 within three layers. The matrix material is a resin with Young's modulus 5000 MPa and Poisson's ratio 0.3. The yarn structure is of material defined by Young's modulus of value 100 MPa and Poisson's ratio 0.3 The RVE has a dimension $[1 \times 1 \times 0.25]$ mm.

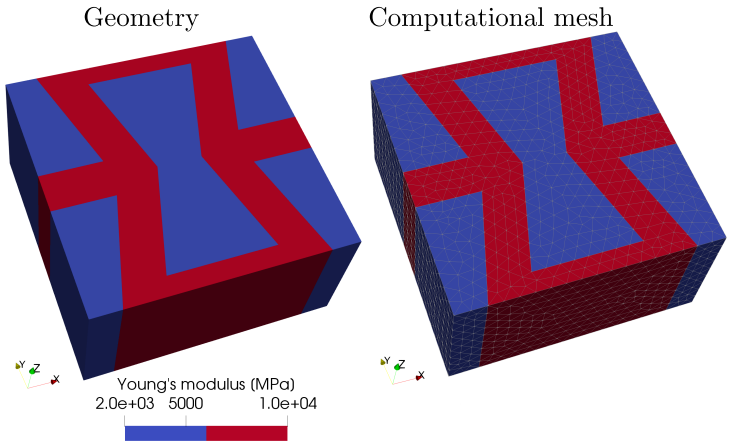

Figure 1.12: The RVE composite with meta-material structure defined by auxetic pattern.

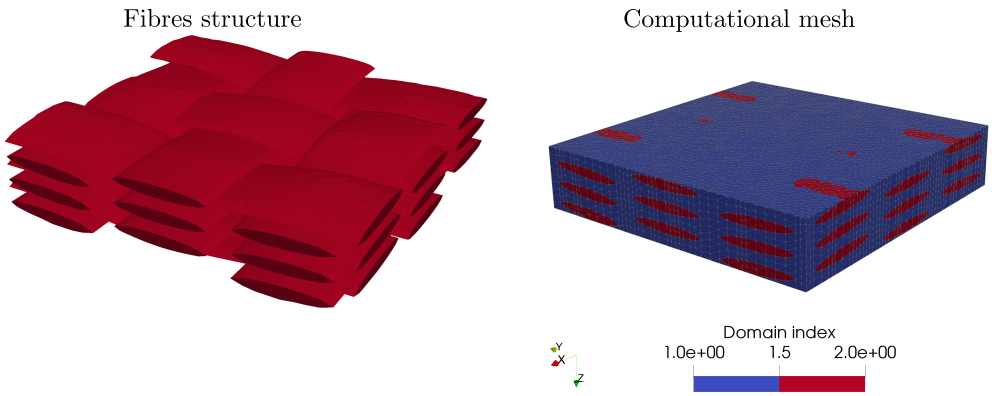

Figure 1.13: The textile composite RVE defined with simple woven structure. The geometry and mesh were created in the software TexGen [10].

1.9 Results

1.9.1 Convergence Analysis of Nitsche's Method

The convergence analysis for the Nitche method (Figure 1.14) shows considerable errors in the jump operator norm L^2 and shear stress H^1. Refining the mesh reduces these errors for a suitably chosen stabilisation parameter, β. The optimal stabilisation parameter value must be estimated for Nitche's method. Otherwise, we may obtain unstable, suboptimal solutions or poorly conditioned systems. The latter can deteriorate the convergence rate if the stabilisation parameter is too high. Figure 1.15 shows the stress distribu-

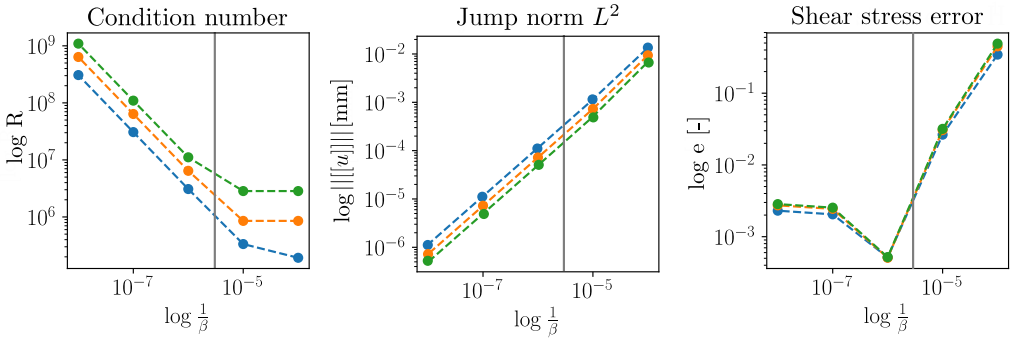

Figure 1.14: Convergence and condition number analyses of the symmetric Nitche method for the shear stress and jump operator norms, including the g_0 term, using h-refinement. The blue, orange and green data are for 1211, 19300 and 53694 DOFs, respectively. The vertical lines show the parameter value estimated via a global eigenvalue-based analysis.

tions for all three methods as we h-refine the boundary mesh three times on the positive sides. The maximum displacement difference found between the mortar and Nitsche solutions is 0.0001%. Nitche's method shows the highest stress difference (0.016%), while the polynomial model shows the lowest stress difference (0.0038%).

1.9.2 Evaluation of Size Effect on Homogenised Elasticity Matrix

The homogenised constant elasticity tensors for the three approaches are listed in Table 1.1. Again, Nitsche's method shows the highest error difference (0.18% for C_{1122}), while the polynomial model shows the smallest error difference (0.005% for C_{2222}).

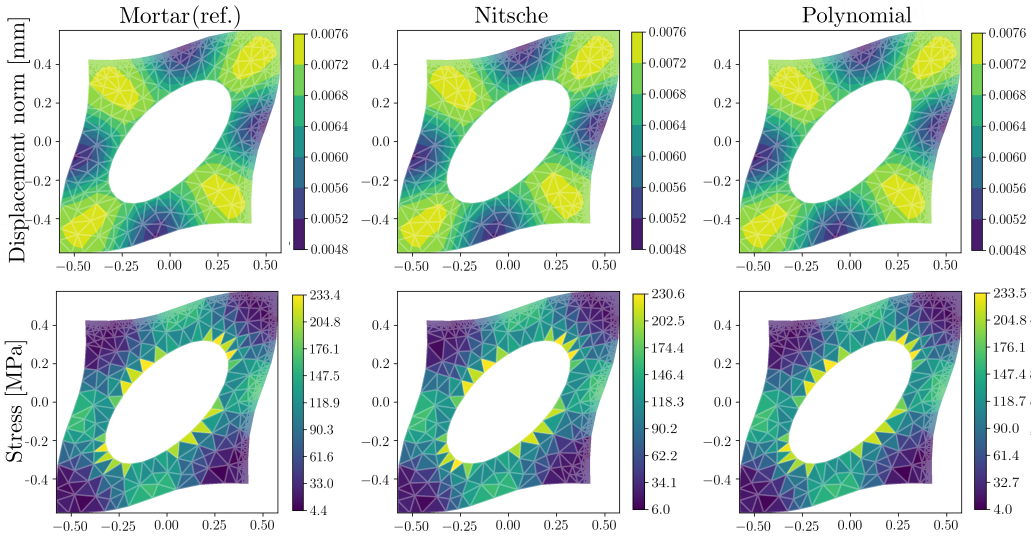

Figure 1.15: Effect of uniform mesh refinement of the positive boundaries on the displacement and von Mises stress distributions. The initial mesh size is $\frac{l_{ref}}{25}$ and the final size is $\frac{l_{ref}}{100}$. The stabilisation parameter was 5.01^{-5}.

Table 1.1: Homogenised isotropic elasticity tensors $\mathbb{C}$ for the three methods.

Mortar (ref.)

$$\begin{bmatrix} 15489.11 & 6536.23 & 0.01 \\ 6536.23 & 15488.81 & 0.02 \\ 0.01 & 0.02 & 4475.01 \end{bmatrix}$$

Nitsche

$$\begin{bmatrix} 15482.36 & 6524.21 & 0.01 \\ 6524.21 & 15480.87 & 0.02 \\ 0.01 & 0.02 & 4479.02 \end{bmatrix}$$

Polynomial

$$\begin{bmatrix} 15487.87 & 6535.33 & 0.02 \\ 6535.33 & 15487.93 & 0.02 \\ 0.02 & 0.02 & 4476.68 \end{bmatrix}$$

Figure 1.16 shows how all three methods' elastic properties converged, indicating that the elasticity tensor values usually stabilise after the RVE scale has been increased three times.

1.9.3 Two-Scale Analysis Results

The stresses on the loaded beam at both the micro- and macro-scales are shown in Figure 1.17. This indicates that the jump operator error is lower for Nitsche's method than for the reference mortar method, while the stress error is up to 0.007%. The micro-scale stress error distributions were similar, with errors of around 0.001%–0.007% (not shown).

1.9.4 Evaluation of 3D Models

The Von mises stress distributions for shear unit macro load (the same as for 2D analysis) of 3D linear models is shown in Figure 1.18 at random re-

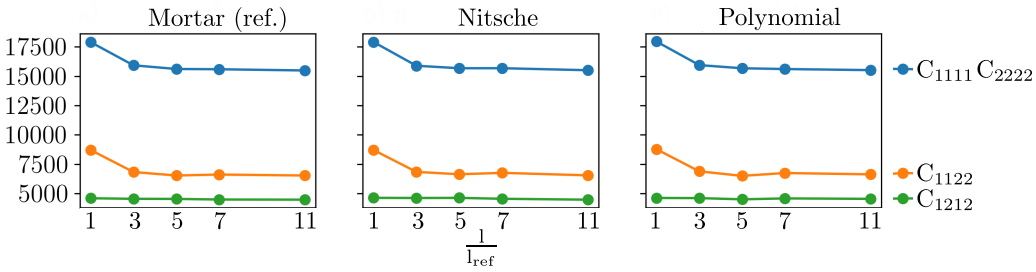

Figure 1.16: Convergence of the elasticity constants with respect to the RVE model scale. These are computed 50 times per scale to obtain average values for the elasticity tensor **C**.

alization if possible. No visual artefacts on boundaries caused by Nitsche discretisation are seen. The stress values are in range 0.3–1400 MPa, although could not be physically representative because of too high macro load (for linear models such those it is even irrelevant because the linearity assumption causes the resultant homogenized properties independent on macro load). The poly-crystal structure **RVE3D-CR** stress magnitudes are correctly the highest as its material phases are highly stiff with respect to the other models. The **RVE3D-I** stress distribution is mostly located around the inclusions with the maximal values of stress 77 MPa. The minimal values of stress are located at matrix and has value 9.9 MPa. The meta-composite model **RVE3D-META** contains complex stress pattern inside the auxetic structure. The maximum stress value is located on boundaries of auxetic structure and has value 37 MPa. The minimum value of stress is again at matrix phase and has value 6.1 MPa. The last textile composite model **RVE3D-TEX** contains the lowest stress (0.3 MPa) inside of woven fabric as it less stiff than matrix phase. The maximum stress is on the matrix phase boundary and has value 37 MPa. The homogenized elasticity constants depending on the number of cells XY-repetitions are showed in Figure 1.19 for each 3D model. The homogenized elasticity components converge after 3-5 scale magnification. The sufficient number of realisation for the RVEs **RVE3D-CR** and **RVE3D-I** was 100 to get convergent mean and standard values. The models **RVE3D-CR** and **RVE3D-I** show an isotropic material orientation unlike the RVEs **RVE3D-META** and **RVE3D-TEX** which are highly anisotropic as elasticity constant are highly scattered (see Table 1.2). With respect to the other methods (ie, mortar and polynomial), the resultant differences at homogenized properties are at most 0.91% for the between polynomial and Nitsche's methods on elasticity member C_{2323}.

Table 1.2: The homogenized isotropic elasticity tensor $\mathbb{C}$ for 3D RVEs

RVE3D-CR

$$\begin{bmatrix} 254412 & 108882 & 108886 & -24 & 8 & -9 \\ 108882 & 254268 & 108853 & -29 & 4 & 7 \\ 108886 & 108853 & 254330 & 25 & -3 & -22 \\ 24 & -29 & 25 & 72753 & -7 & -5 \\ 8 & 4 & -3 & -7 & 72739 & -16 \\ -9 & 7 & -22 & -5 & -16 & 72747 \end{bmatrix}$$

RVE3D-I

$$\begin{bmatrix} 9201.25 & 3708.53 & 3701.36 & 1.29 & 2.85 & 2.89 \\ 3708.53 & 9153.84 & 3681.99 & 4.23 & 3.74 & 3.22 \\ 3701.36 & 3681.99 & 9123.63 & 4.21 & -0.25 & 1.03 \\ 1.29 & 4.23 & 4.21 & 2725.36 & -12.45 & 1.45 \\ 2.85 & 3.74 & -0.25 & -12.45 & 2720.01 & 3.76 \\ 2.89 & 3.22 & 1.03 & 1.45 & 3.76 & 2722.78 \end{bmatrix}$$

RVE3D-META

$$\begin{bmatrix} 4898.19 & -1829.17 & 2018.14 & -1.03 & -0.46 & -2.06 \\ -1829.17 & 5969.72 & 2340.74 & -2.76 & -0.01 & 0.36 \\ 2018.14 & 2340.74 & 6921.14 & -0.24 & -0.80 & 0.24 \\ -1.03 & -2.76 & -0.24 & 1288.13 & -0.20 & 1.08 \\ -0.46 & -0.01 & -0.80 & -0.20 & 1876.7 & 0.87 \\ -2.06 & 0.36 & 0.24 & 1.08 & 0.87 & 1505.01 \end{bmatrix}$$

RVE3D-TEX

$$\begin{bmatrix} 842.11 & 240.99 & 137.87 & -2.66 & -0.14 & 1.18 \\ 240.99 & 842.64 & 138.62 & -3.48 & 0.43 & 1.39 \\ 137.87 & 138.62 & 411.32 & -1.64 & 0.27 & 0.42 \\ -2.66 & -3.48 & -1.64 & 228.50 & -0.59 & 0.62 \\ -0.14 & 0.43 & 0.27 & -0.59 & 112.65 & 0.48 \\ 1.18 & 1.39 & 0.42 & 0.62 & 0.48 & 110.49 \end{bmatrix}$$

1.9.5 Evaluation of Boundary Flux with Generalized Gradient Mapping

The norm of difference of normal flux computed by standard mapping method and the proposed in section 1.7 is show in Table 1.3. The mesh size density was the same for all models as the results are mesh size dependent and with refining the mesh, the norm difference decreases. The resultant norm of difference is in range from 5.1^{-10} to 8.9^{-7}. Except **RVE2D-H**,**2SC2D-BI**, **RVE3D-META** and **RVE3D-TEX**, the results are mean values as comm from multiple stochastic realizations. Nevertheless, the **2SC2D-BI** has no statistical meaning, as it is only spatial average on macro-scale model related to Figures 1.7 and 1.17.

Table 1.3: Norm of normal flux difference for common and generalized mapping scheme for three periodicity directions $\mathcal{A}$. Norm is computed at the mesh density($\frac{10}{l_{ref}}$) of RVE.

	2D			3D			
$\mathcal{A}$	**RVE2D-H**	**RVE2D-I**	**2SC2D-BI**	**RVE3D-CR**	**RVE3D-I**	**RVE3D-META**	**RVE3D-TEX**
x	1.1^{-8}	2.5^{-9}	3.1^{-8}	0.2^{-8}	5.1^{-10}	3.6^{-9}	5.1^{-8}
y	8.9^{-7}	8.1^{-8}	3.4^{-8}	3.6^{-9}	5.1^{-8}	2.7^{-9}	6.2^{-8}
z	-	-	-	9.4^{-8}	7.1^{-8}	1.3^{-8}	4.7^{-8}

1.9.6 Penalty/Nitsche Stabilization Parameters Interaction

For more complex bilinear forms arising from complex underlying physics, a mix of Nitsche, Lagrange multipliers or penalty terms can occur. Although the Nitsche method is well documented, studies usually do not treat more terms and their interaction to the author's knowledge. In this sub-study the

only numerical evaluation of penalty/Nitsche terms is introduced[4]. Recall the bilinear form split up to bulk and Nitsche terms:

$$a(\mathbf{u},\mathbf{v}) = [a(\mathbf{u},\mathbf{v})_{bulk} + \beta_1 a(\mathbf{u},\mathbf{v})_{rmr}] + [a(\mathbf{u},\mathbf{v})_{Nitsche} + \beta_2 a(\mathbf{u},\mathbf{v})_{pen}] \quad (1.65)$$

From stability analysis we already know that bulk form must be already coercive to get meaningful bound for Nitsche term. Bulk form is not well posed unless the rigid body translation is removed. Injecting the penalty term that ensures the average displacement fluctuation is zero, we can assume a relation $\beta_2 = \mathrm{f}(\beta_1, ...)$. Consider the 3D RVE with one material phase for reference and model **RVE3D-META**. The load is the same as in section 1.8. The stabilisation parameter $\frac{1}{\beta_1}$ is of range $1 - 10^{10}$. The response of a reference 3D model is given on the Figure 1.20. The homogenised shear stress value is stable up to 10^5, after quickly deteriorates. Jump norm is the lowest(also the visual distribution has a regular pattern) for small values of penalty parameter $\frac{1}{\beta_1}$ up to value 10^3, after that threshold, the jump norm is increasing. The eigen-value representing the stabilisation parameter $\frac{1}{\beta_2}$ starts with value 10^7 at lowest values of parameter in figure $\frac{1}{\beta_1}$. The eigen-value gradually decrease up to values 10^2. The conditions number of stiffness matrix decreases with increasing the $\frac{1}{\beta_1}$ up to value 10^6, where start increasing. Considering more complex model **RVE3D-META**, we get its response for different $\frac{1}{\beta_1}$ on Figure 1.21. The shear stress of value 15.27 MPa is stable with small fluctuation up to limit value 10^9. The displacement field jump tends to increase with increasing the stab. parameter unlike the estimated eigenvalue and condition number which decrease. Nevertheless, material inhomogeneities and mesh anisotropy deteriorate the efficiency of the globally estimated mesh dependent constant based on the eigenvalue analysis. More likely, the stability parameter can be estimated as an estimate weighted by the material constants. Having the constant strain triangle/tetrahedra, the local estimate of stab. parameter at closed form can be estimated [105], later extended for non constant Jacobian by Owens in [81]. To overcome the material heterogeneities an approach based on the work of Annavarapu [4] is introduced. Recall the weighting parameter γ from section 1.2.2 and notice that $\gamma_- + \gamma_+ = 1, \gamma_- = \gamma$. The stabilisation parameter C^2 can be estimated with help of characteristic measures (operator $meas(\cdot)$) on interface Γ_I and

[4]Numerical results should be interpreted in a more rigorous mathematical way, nevertheless it is over the scope of the purpose of this study.

adjacent cells Ω_e:

$$\mathbf{C}^2 = meas(\Gamma_I)\left(\frac{||\mathbb{C}_e^1||(\gamma_e^1)^2}{meas(\Omega_e^1)} + \frac{||\mathbb{C}_e^2||(\gamma_e^2)^2}{meas(\Omega_e^2)}\right) \tag{1.66}$$

$$\gamma_e^i = \frac{\frac{meas(\Omega_e^i)}{||\mathbb{C}_e^i||}}{\frac{meas(\Omega_e^1)}{||\mathbb{C}_e^1||} + \frac{meas(\Omega_e^2)}{||\mathbb{C}_e^2||}}, i = 1, 2 \tag{1.67}$$

Characteristic measures are defined by the length/area/volume of an interface and interior cells. Combining the expressions in 1.66 we segregate the weighting factors γ^i. The local estimate is used for both normal and tangential components of stabilisation terms in 1.65. Estimating the stabilisation parameter by the weighted sum introduced 1.66, the homogenised material parameters of **RVE3D-META** were correctly computed.

1.9.7 Note on Energy Equivalence and Symmetry of Homogenized elasticity Tensor

Computing components of homogenized elasticity via the average stress operator defined in (1.5) leads to a small asymmetry of the resultant homogenized elasticity tensor. Moreover, the energy equivalence is also maintained less accurately than with (1.57). The homogenized stress tensor computed by (1.5) somehow does not exactly respect the RVE equilibrium due to discretization and hence violates the symmetry of the homogenized elasticity tensor. Nevertheless, the level of symmetry is also somehow influenced by the method used for PBC treatment. The energy equivalence condition defined in (1.6) is most precisely recovered by mortar method, following the interpolation and Nitsche's methods (Table 1.4). The mortar method provides the most accurate recovery of symmetry, followed by interpolation method (Table 1.5). The Nitsche's method accuracy is dependent on the penalty parameter according to auxiliary extensive numerical tests. In comparison with arbitrary com-

Table 1.4: The level of fulfilment for Hill-Mandel conditions for tested methods with $\hat{\mathbf{C}}$ computed with average stress operator (1.5).

Method	subsection 1.8.2	subsection 1.8.4	section 1.8.5
Polynomial	1^{-7}	2^{-7}	3^{-7}
Mortar	1^{-8}	5^{-8}	2^{-8}
Nitsche	1^{-7}	4^{-8}	4^{-7}

puted homogenization tensor according (1.57), the energy equivalence across

Table 1.5: The level of asymmetry expressed as an absolute difference of shear terms $|C_{12} - C_{21}|$ for 2D and $|C_{23} - C_{32}|$ for 3D in homogenized elasticity tensors.

Method	subsection 1.8.2	subsection 1.8.4	section 1.8.5
Polynomial	1.02	0.89	4.2
Mortar	0.01	0.01	2.3
Nitsche	0.92	0.81	5.1

the scales is accurately maintained for all tested PBC treatment methods (the total energy density difference was 1^{-16}). Further, the symmetry of homogenized tensor is maintained absolutely.

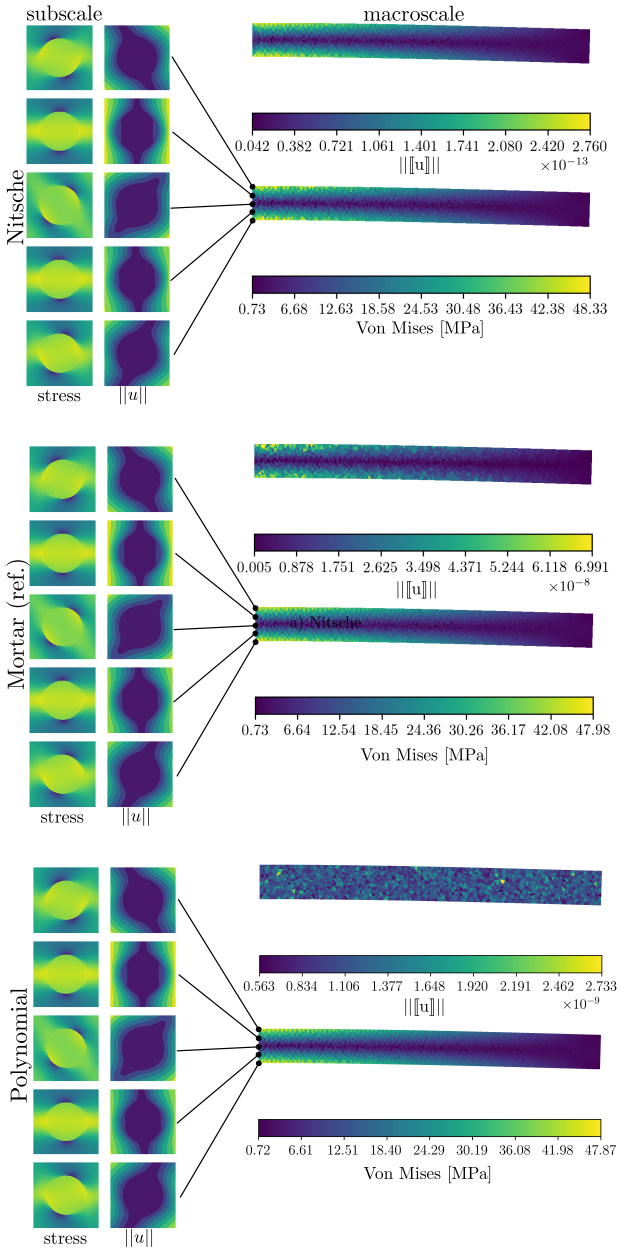

Figure 1.17: Convergence of the jump operator and von Mises stress distributions for the two-scale beam analysis. The stabilisation parameter for Nitsche's method was 7.3^{-7}.

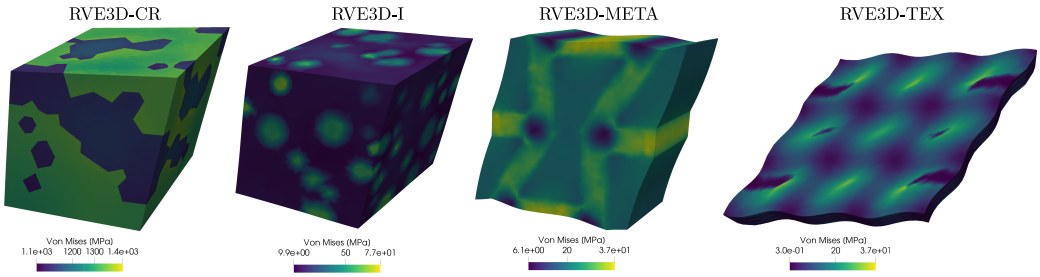

Figure 1.18: An evaluation of stress distribution for 3D RVEs models. The deformation is magnified 30 times.

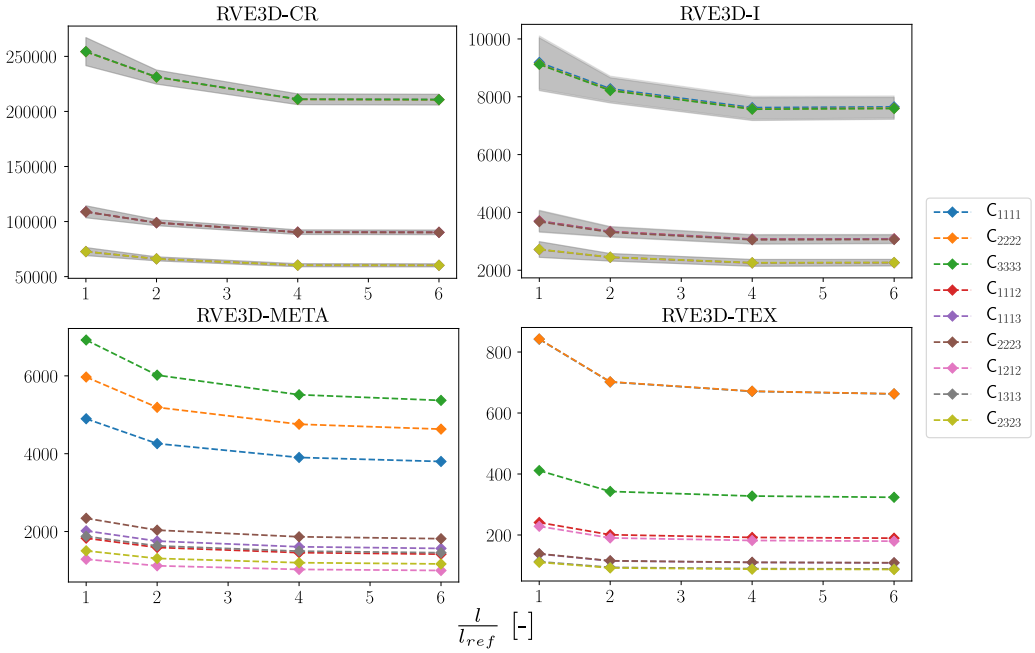

Figure 1.19: The evaluation of elasticity constant for different 3D RVE models with estimated mean and standard values where was is possible. The grey fill expresses the 95 % confidence intervals.

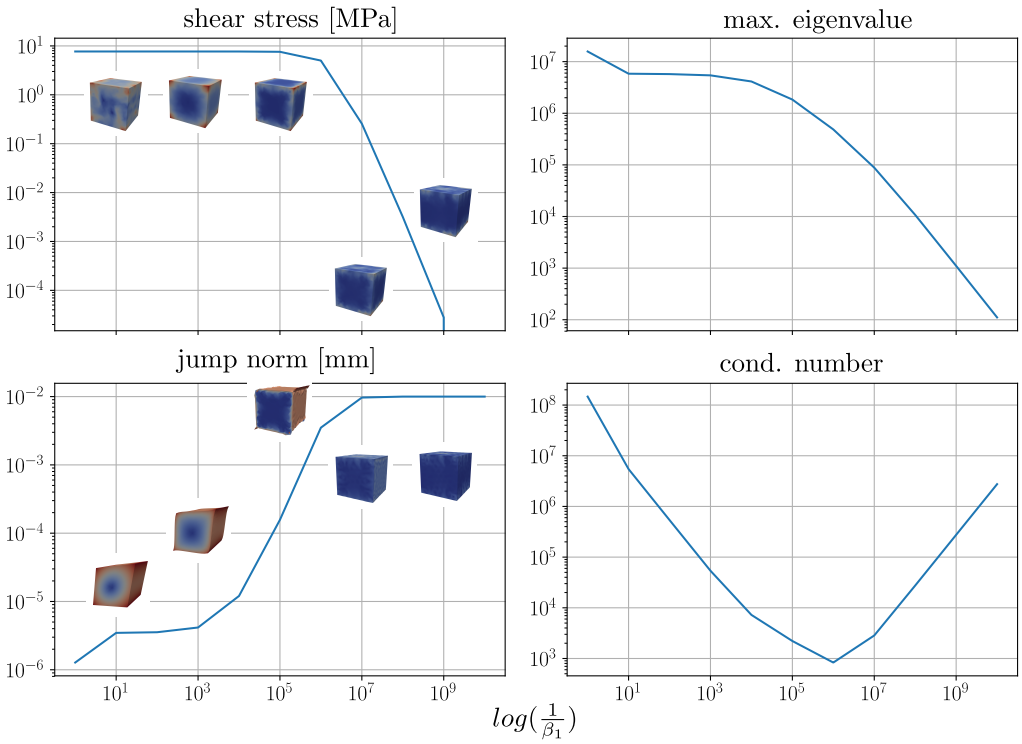

Figure 1.20: Dependency of important variables defined (reference model with homogeneous geometry and material distribution) on the penalty parameter associated with the constraint integral removing the rigid translations. Eigenvalue corresponds to a maximal value given by the global stabilisation estimate from subsection 1.2.3. The zero parameter is not considered. Quick shots of the Von mises stress and displacement norm fields are shown for sudden penalty parameters.

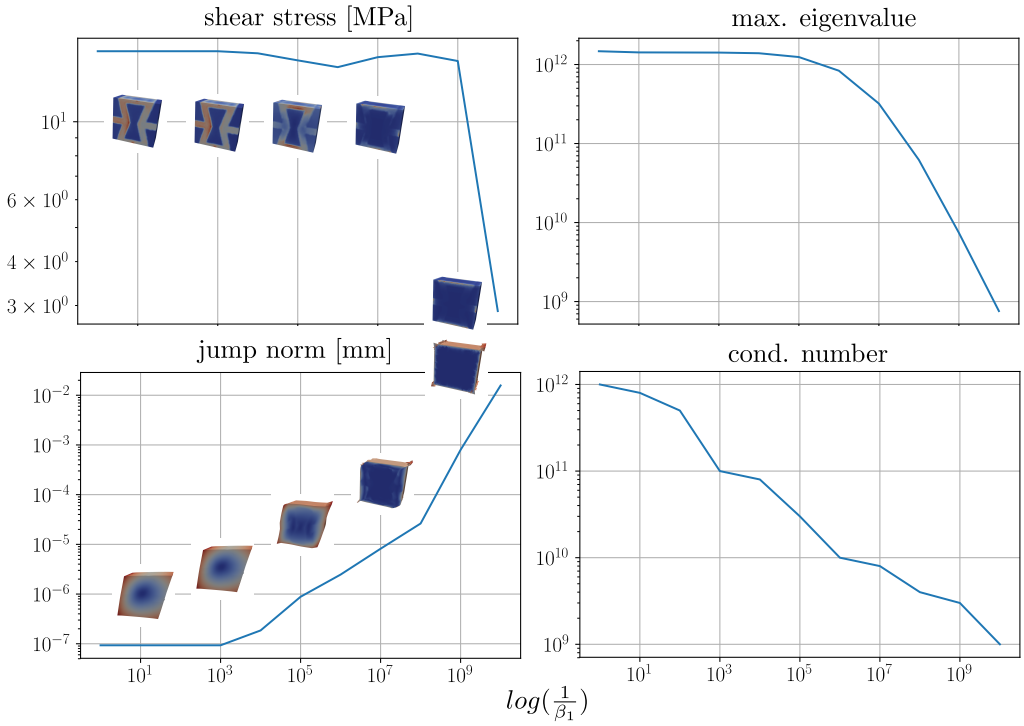

Figure 1.21: Dependency of important variables defined (**RVE3D-META**) on the penalty parameter associated with the constraint integral removing the rigid translations. Eigenvalue corresponds to a maximal value given by the global stabilisation estimate from subsection 1.2.3. The zero parameter is not considered. Quick shots of the Von mises stress and displacement norm fields are shown for sudden penalty parameters.

1.10 Discussion on Implementation of Periodic Boundary Conditions

Periodicity conditions play important roles in micro-mechanical analyses and the multi-scale approach. Although these constraints can be trivially fulfilled for periodic meshes, the non-periodic case is far less straightforward. For complicated morphologies (e.g. geometry CT-based data) the conformal mesh boundaries present a challenge. Most of the methods developed to enforce PBCs are either meshless or mesh-based. This study considered one meshless method (interpolation with Hermite polynomials) and two weak mesh-based methods. Table 1.6 summarises the performance of the tested methods. Although our evaluation could be seen as somewhat subjective, we have nevertheless tried to objectively examine and highlight the methods' most important properties and provide recommendations to support the decision-making process. Our convergence analysis focused on the jump

Table 1.6: Overall evaluation of the tested methods.

Method	Convergence	Accuracy	Addnl. DOFs	Solver	Addnl. params	Impl. complexity
Poly.	Good	Good	No	Regular	Order	Good
Mortar	Good	Good	Yes*	Direct*	Inf–sup**	Average
Nitsche	Good	Good	No	Regular***	Stab. param.****	Average

* Can be eliminated to obtain a purely displacement-based formulation.
** A stable mixed scheme must be provided.
*** The form can be unsymmetric, in which case the regular conjugate gradient method fails.
**** Stabilisation parameter estimation requires potentially an additional solution step.

operators, showing that all the methods converge under optimal conditions. The interpolation method's accuracy is bounded by the particular method used. For example, higher-order interpolation may be required if the boundary deformation is complex (i.e., the RVE geometry is complex), in which case the oscillations of Lagrange polynomials cause a loss of accuracy. On the other hand, using a low-order Lagrange polynomial again leads to a loss of accuracy up to first order, recovering linear displacement boundary conditions. Given that Lagrange polynomials are not suitable for higher-order interpolation, alternatives, such as splines or the Hermite polynomials used in this study, may be preferable.

From an efficiency point of view, the interpolation method augments the underlying FE formulation. It requires cell-wise construction of specific transformation matrices and multiplication during the assembly process. This additional step decreases computational efficiency and hence requires considerable effort to achieve good model performance. On the other hand the constrained DOFs can be replaced by a few global DOFs, considerably reducing the size of the system to be solved. While it has a negative impact

on FE matrix sparsity pattern, this effect is not significant to the best of our knowledge (which is consistent with the findings of [74]). Solver time of the linear system originates from interpolation method was up to 8 % higher than the solver time for Nitsche's method in our examples. An advantage of this method is that maintains periodicity for boundaries containing voids. Nitsche's method omits the Lagrange multipliers, replacing them with the boundary flux. This means the system can be efficiently solved by the conjugate gradient method and without additional DOFs, in contrast to the mortar approach where the final matrix has zero values on its diagonal and contains additional DOFs in terms of Lagrange multipliers. However, Nitsche's method still involves computing the gradient on the boundary. Although this can be automated by algorithmic differentiation, it potentially increases the implementation complexity.

The accuracies of the mortar and Nitsche methods are excellent (again under optimal conditions). Both of these methods need an accurate integration scheme for non-matching interfaces. This is an even more challenging requirement in 3D space, where polygon clipping and further triangulation of the projected polygon are needed [92, 20]. There is an alternative approach that only projects the non-mortar Gauss integration points onto mortar side, but this may involve a possible loss of accuracy [108]. The mortar method requires a stable discretisation scheme that fulfils inf–sup conditions [106], so it depends on the nature of the underlying partial differential equations and fields computed. Another drawback is that the Lagrange multipliers increase the number of DOFs that must be solved. Fortunately, discretising the Lagrange multipliers using a bi-orthonormal basis allows them to be effectively eliminated from the system solution, although the inf–sup conditions are still required [92, 33].

This most significant drawback of Nitsche method is that it usually requires an estimated stabilisation parameter in order to achieve a coercive bilinear form. As we have noted in this study, however, this can be partly avoided by considering an unsymmetric variant of the method or by estimating the stabilisation parameter [4, 78]. Although this variant is consistent with the form used in previous studies [32, 13, 49], we have only focused on the symmetric one in this study, as it is better known. In addition, Nitsche's method is central to cut FE/multimesh methods, which have great potential for alleviating the mesh burden as they allow the background (matrix) and inclusion meshes to be generated separately [11, 69].

All the methods tested in this study provide excellent accuracy and no one method significantly outperforms the others. The mortar and Nitsche methods are well known and widely used in contact mechanics and domain decomposition techniques [108, 106]. To the best of our knowledge, however,

only the interpolation method has been used for second-order homogenisation [75]. There are no documented examples of the mortar or Nitsche methods being used to enforce periodicity in second-order homogenisation, but we can see no obvious limitations to their use in this area.

One drawback of this study is that the methods were only tested using simple benchmarks, which might not have revealed all the details. Studying the application of these methods to high-order/XFEM discretisation [6, 7] or the complicated multi-physical phenomena needed for multi-scale simulations can be challenging, and using them to enforce complex field periodicity is not well documented, although the mortar and Nitsche methods have been studied for high-order discretisation and multi-physical coupling [17, 44, 21, 96]. This, however, lies beyond the scope of this study, which was to review interpolation- and mesh-based methods and propose a new approach based on Nitsche's method.

Apparently, the globally estimated stabilisation parameter for the Nitsche's method is not robust. In the case of multi-material structures such were tested in this study, the maximal eigen-value overestimates systematic the optimal stabilisation parameter, especially with larger material contrast. It leads to badly conditioned system hardly solvable with inaccurate output. Fortunately, locally estimated material coefficient-weighted estimation of stabilisation parameter can be applied (see 1.66 explored in study [4]). Including the additional constraint to remove rigid body translation via the penalty method, a specific interaction between two stabilisation parameters occurred, not described in the literature. Numerical experiments show that small values of $\frac{1}{\beta_1}$ negatively influence the conditioning of the system and increasing the estimated $\frac{1}{\beta_2}$ parameter, nevertheless the macro stress, tangent and jump norm are of good accuracy and relative stable up to some limit point (for homogeneous material box it was 10) at small values of $\frac{1}{\beta_1}$ close to zero. Moreover, the macro stress and tangent stiffness are computable at zero valued $\frac{1}{\beta_1}$. Interaction of two stabilisation parameters at one bilinear form form is not linear and contains some critical points (see the Figure 1.20, 1.21). To solve complex engineering tasks, no one can expect simple PDEs with only one constraints and hence a robust estimation of stabilisation parameters should be provided.

Despite the discussed limitations of Nitche's method, the fact is it an intensively studied, and definitely yet not completely explored method to consistently, with a posterior error estimate, treat the constraints.

The implementation highlight for Nitche's method is an integration on the skeleton. Integrating of the primal variable on the boundary is straightforward and technically well treatable algorithm. Nevertheless the integration

of the gradient is usually treated by the additional mapping on between the given element topology objects (tetras-¿triangles-¿edges). The standard isoparametric mapping is now well defined, as it maps at two objects of different dimensions. Exploiting the curvilinear formulation ad proper defining the covariant/contravariant metric one can elegantly transform the gradient in a common way known for isoparametric mapping with no loss of accuracy.

Chapter 2

Gradient Smoothed Homogenisation

2.1 Introduction

Modern materials contain precisely designed microstructures with one or more constituent phases. Controlled and tuneable microstructures allows us to produce materials with multifunctionality, light weight and high mechanical performance. The key step to achieve high-performance materials is the design of the microstructures. However, it is difficult to find the most effective structure and evaluate it by either an experimental or a computational approach. Investigating the material effective properties has been of great interest in the scientific community for decades. One of the first attempts related to the analysis of a composite material was to obtain its analytical material bounds (Hashin–Shtrikman bounds) [34]. Although this is effective, in an analytical model, the geometrical characteristics of the material are not incorporated.

Computational homogenisation is a popular method for computing the effective properties of media, including composite materials [40, 1, 25, 71, 3] or for other multiphysics of fluids [97, 55] or heat transfer [83, 82]. A computational model is represented by representative volume elements (RVEs) or unit cells. The model is repeated, and periodicity is often required. Homogenisation is based on rigorous mathematical theory and allows for the design of a material from its microstructure [31, 8]. The FE method is often used in computational homogenisation, which is significantly used in composite microstructural design [40, 1, 25, 71, 3]. Conformal displacement-based FE is commonly used because of its computational efficiency as the regular low-order FE method suffers from overly stiff results [115], mesh distortion

sensitivity and poor gradient reconstruction accuracy, which is approximated via piecewise linear functions [64, 65]. These issues certainly deteriorate the performance and accuracy of micromechanical FE mode RVEs, which were used to compute the mechanical response herein. To overcome the aforementioned limitations, the *gradient (strain)*-smoothing technique is studied herein. The basic idea of the method is that the compatible strain is replaced by its smoothed counterpart. The computational domain now contains domain subdivisions based on the FE mesh topology. The main feature is that gradient evaluation is no longer performed at nodal points but on the subdomain boundaries. This has been made possible by the divergence theorem. In fact, the method originated from the stabilised conforming nodal integration (SCNI) introduced in previous research [12]. Depending on the construction of the smoothing subdomains, we recognise the following: cell (**CS-FEM**), face (**FS-FEM**), edge (**ES-FEM**) and node (**NS-FEM**)-based smoothed FE method [60, 61, 77, 63, 62, 35, 36]. These variants provide unique properties that superior to those of the regular FE method:

1. Accuracy
2. Upper/lower bound on material properties
3. Mesh quality insensitivity
4. Spurious energy mode suppressions
5. Soft response (less stiff)

We only considered the ES-FEM variant as it is more suitable for the homogenisation method in mechanical engineering (this decision has been supported in a previous study [57]). Although homogenisation on linear elastic frameworks has been investigated in previous research [57] with good examples of the importance of S-FEM in homogenisation, more complex computational models involving the important periodicity constraints on non-matching boundaries should be established. This study aimed to improve the standard homogenisation method by smoothing the gradient field discretised by the linear FE method, including various formulations of periodic boundary conditions. A conformal mesh cannot be always obtained because of geometrical and material complexity, and therefore, tying the opposite boundaries of the RVEs is generally required. To treat the periodicity conditions in non-conformal RVEs, we implement Mortar and Nitsche's methods and discuss their interaction with smoothed FE formulation.

2.2 Smoothing Gradient Formulation

Considering the elasticity problem formulated in sections 1.2 and 1.3, we select strain $\boldsymbol{\varepsilon}$ and smooth it over the smoothing domain Ω^k as follows:

$$\bar{\boldsymbol{\varepsilon}}(x) = \int_{\Omega^k} \boldsymbol{\varepsilon}(x)\Phi(x)\ \mathrm{d}\Omega. \tag{2.1}$$

The weighting function $\Phi(x)$ can be chosen as

$$\Phi(x) = \begin{cases} \frac{1}{A_k} & x \in \Omega_k \\ 0 & x \notin \Omega_k, \end{cases} \tag{2.2}$$

where A_k is the area of the smoothing subdomain. Furthermore, the weighting function should fulfil the compactness and

$$\int_{\Omega_k} \Phi(x)\ \mathrm{d}\Omega = 1, \Phi > 0. \tag{2.3}$$

By employing the divergence theorem, we can rewrite Eq. (2.1) in terms of outer normals $\mathbf{n}_k$ and primal variable displacement $\mathbf{u}_k$

$$\bar{\boldsymbol{\varepsilon}} = \frac{1}{A_k} \int_{\Gamma_k} \mathbf{n}_k \otimes \mathbf{u}_k\ \mathrm{d}\Gamma \tag{2.4}$$

on the boundaries of the smoothing subdomain. The divergence trick allows us to generalise smoothing by n-sided polygonal elements. To continue, the smoothing subdomains must be constructed. In Figure 2.1, a 2D triangular RVE mesh is shown. Based on the mesh topology, the triangle midpoints *cp* and edge intersection points *ip* of the smoothing domains are built. The computational mesh now contains the triangle midpoints cp_j^k. The index k describes the smoothing subdomain, index j and its subdomain. Interior smoothing domains contain two adjacent subdomains Ω_j^k inferred from the two adjacent triangles. The boundary edges contain only one adjacent triangle and therefore only one smoothing subdomain. The smoothed edge always contains two nodal points $p_i, j \leq i$.

Having defined the smoothing domains on the domain edges, common P1 approximation functions $\psi(x)$ are defined on the edges in a matrix form $\mathbf{N}(x)$. On employing the Voigt notation, we can write the k$^{\text{th}}$-smoothed gradient matrix as

$$\bar{\mathbf{B}}_\Gamma^k = \frac{1}{A_k} \sum_{i=1}^{S} \mathbf{n}_i(x)\mathbf{N}_i(x)l_m, \tag{2.5}$$

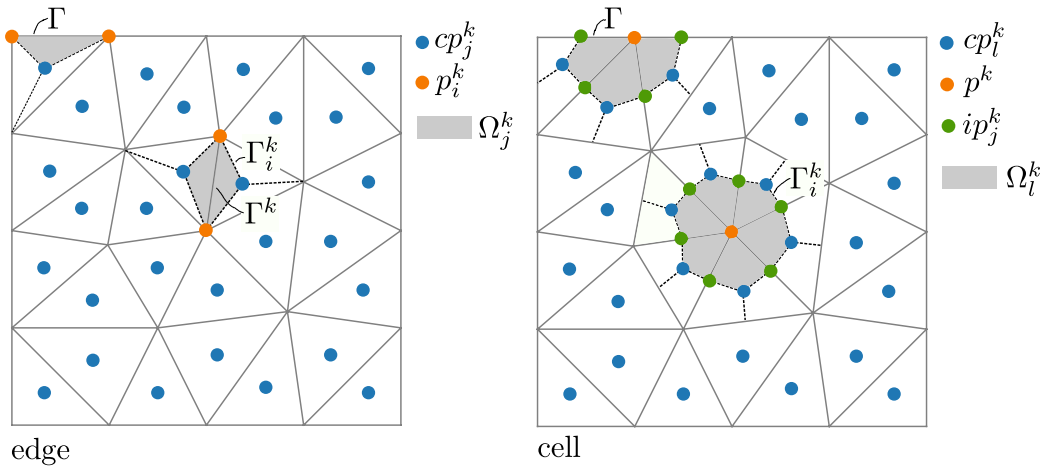

Figure 2.1: Geometrical domains and ES-/CS-FEM smoothing subdomains.

where the variable l_i is the subdomain edge length. The summation is performed over all boundary edges of the subdomains; thus, the interior S = 4 and the RVE boundary S = 2. The final bulk stiffness matrix is assembled as

$$\bar{\mathbf{K}} = \bigcup_{k=1}^{N_k} \bar{\mathbf{B}}_k^T \mathbb{C} \bar{\mathbf{B}}_k A_k \tag{2.6}$$

over the all domain edges N_k. The shape functions $\psi(x)$ are evaluated at Gauss points on the edges of the smoothing subdomains. Replacing the strain–displacement matrix $\mathbf{B}$ by a smoothed one from the ES-FE method, we can obtain a more accurate solution with suitable properties for the first-order linear discretisation on the triangular irregular mesh. When a constant strain triangular elements are used, the following alternative form of smoothed gradient matrix can be used

$$\bar{\mathbf{B}}_\Gamma^k = \frac{1}{A_k} \sum_{p=1}^{S_p^e} \frac{1}{3} A_p^e \mathbf{B}_p^e \tag{2.7}$$

where S_p^e is the number of elements sharing the edge k, A_p^e is the are of the triangular element associated with edge k and $\mathbf{B}_p^e$ is the standard compatible strain-displacement matrix of triangular element. The alternative formulation is called "average" in the results.

2.3 Benchmark Setup

The benchmark in this chapter shows that the elasticity constant obtained from homogenisation converges faster to the nominal values and that the overall model is not too sensitive to mesh distortion. Special attention is given to the dynamic properties of the structure and wave propagation because according to the literature, they are the fields wherein **ESFEM** gives significantly better results than a standard formulation of the FE method [110, 37]. Consider the microscale model defined as a square (1 mm × 1 mm) reference cell with a hole of radius r (0.2–0.45 mm). The material is linear elastic described by the Young's modulus E = 1000 MPa and Poisson's ratio of 0.3 [-]. To demonstrate better convergence with the dynamic application of the smoothed formulation, modal analysis was performed with structural density $\rho = 1000\frac{kg}{m^3}$. The generalised eigenvalue problem was solved using a consistent mass matrix. The Krylov–Schur method, together with the spectral shift transform, was used to find the five lowest deformable modes. Spectral transformation was solved by auxiliary defined factorisation using the MUMPS solver (PETSc/SLEPc libraries [5, 38, 2]). All modes were normalised with respect to the mass matrix. Only the bulk form was used, as a full periodicity formulation was not required to be obtained along with the rigid constraints. The convergence of Young's modulus E_{11} with respect to reference one was also studied.

2.4 Results

2.4.1 High Porosity Ratio

Having a unit cell with a large hole radius (Figure 2.2 - right/top), the periodic boundary conditions together with the smoothed formulation provided a much more accurate solution (error: ≈10%). However, the kinematic boundary conditions greatly overestimated the Young's modulus. There is a critical necessity to estimate the most efficient number of reference cell replications (i.e. size effect). In Figure 2.2 left/top, the kinematic boundary condition results are more accurate as the number of cells increases. However, depending on cell structure, the number of repetitions grows significantly (5 to obtain sufficient results in our case; Figure 2.2 middle/bottom). With decreasing hole radius (Figure 2.2 left/right/middle), the results of the kinematic BCs converge with a bias smaller than that in the case of high porosity.

2.4.2 Smoothed vs Regular Periodicity

A comparison of the results for the PBCs shows that the smoothed formulation converges faster and needs fewer repetitions (two versus three) of the reference cells (Figure 2.2). Both formulations are much less sensitive to the number of cells than kinematic BCs. The results differ in the worst case by ≈11% (Figure 2.2 bottom). Similar patterns can also be found for the shear stress, where the values differ even less (≈7%, Figure 2.3).

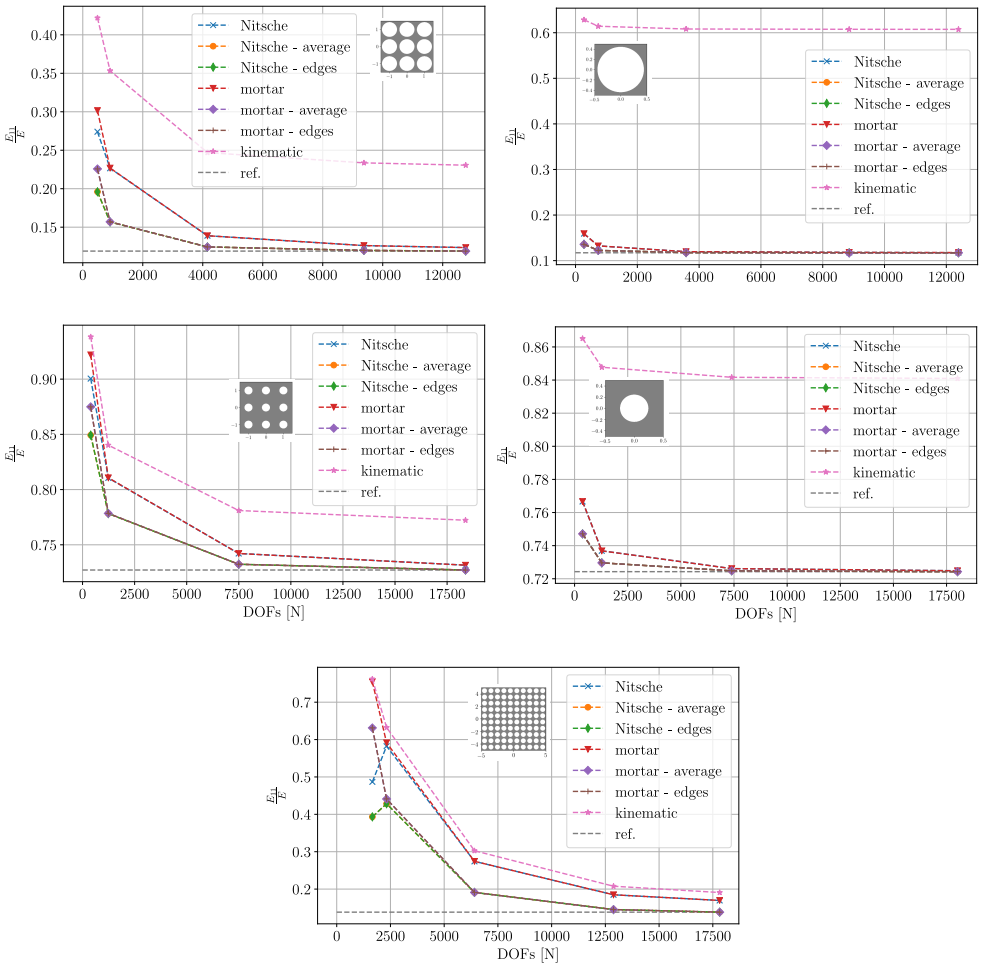

Figure 2.2: Convergence of E_{11} for various configurations of the RVE model.

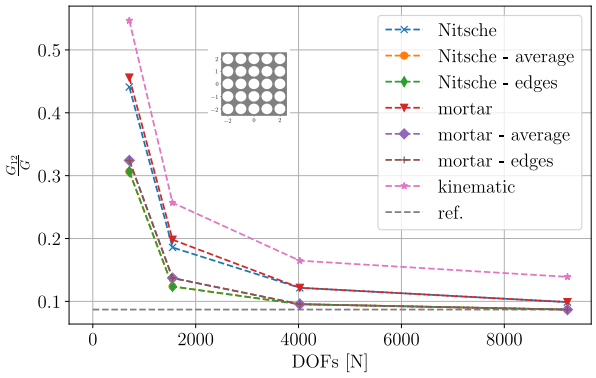

Figure 2.3: Convergence of G_{12} for specific configurations of the RVE model.

2.4.3 Eigenvalues

The convergence of the eigenfrequencies is shown in Figure 2.4. The first two shapes are bending-/shearing-like modes. The third and fourth shapes are some combination of the first two and are symmetric. The last shape is a torsion-like mode. The corresponding eigenfrequencies converge faster and to a less 'stiff' solution for the smoothed formulation. The highest difference (5%) is at mode 4.

2.5 Discussion

The smoothed FE method provides a robust platform in computational homogenisation as it allows for accurate gradient solutions within the linear FE space. The use of **ESFEM** in the homogenisation mechanics community is seen quite rarely, although **ESFEM** evidently provides a significant increase in the accuracy of the resultant homogenised parameters (both static and dynamic properties). In all tested cases, **ESFEM** outperforms the regular FE method. The advantages of **ESFEM** can be even more significant within a multiscale framework, e.g. FE^2. Nevertheless, this assumption has not yet been tested and can be a basis for future research. All tested methods (mortar and Nitsche at different variants) work well with the smoothed gradient, and additional treatment is usually not required. However, building complex models with mixed FE spaces and smoothing requires inf-sup stability and a coercive final bilinear/semi-linear form. The stabilisation parameter of Nitsche's method was only estimated numerically and globally by computing the maximal eigenvalue associated with the discretised bulk stiffness

and the norm of the boundary flux (see section 1.2.2). Nevertheless, compared with standard FE method formulation, the stabilisation parameter is slightly lower and thus the condition number of the resulting bilinear form is also lower. Periodic boundary conditions were treated by the mortar and Nitsche's methods which are is described in the section 1. Although not rigorous from a mathematical point of view, no substantial compatibility issues were found using the mentioned periodicity implemented together with the smoothed gradient method. Smoothing the gradient would be beneficial for both the mortar and Nitsche's methods as the boundary flux is part of the variational forms. The superior accuracy of ES-FEM is evident, but its efficiency can be somewhat worse or of a magnitude same as that of the regular FE method (see Figure 2.5). In any case, comparing efficiencies is rather subjective and depends on the implementation details. This study focused on a homogenisation analysis in 2D. For comparison, the analogous 3D analysis results should be discussed. The main difference in the 3D analysis can be seen in the more difficult maintenance of periodicity conditions (see the formulations in [20]). Projection of the boundary mesh and integrating on non-matching boundaries require more computational resources ([93] and see subsection 1.8.5). Additionally, in the 3D smoothed model, edge averaging is replaced by face averaging, which does not require additional model corrections with respect to 2D analysis. Computing the boundary flux by introducing Lagrange multipliers on the boundary is known to be inaccurate as the flux is lumped into the nodes; therefore, smoothing the boundary gradient must lead to improved accuracy of the boundary flux. Investigating the smoothed flux only on the boundary within the context of homogenisation and non-matching mesh connections will be studied in future research.

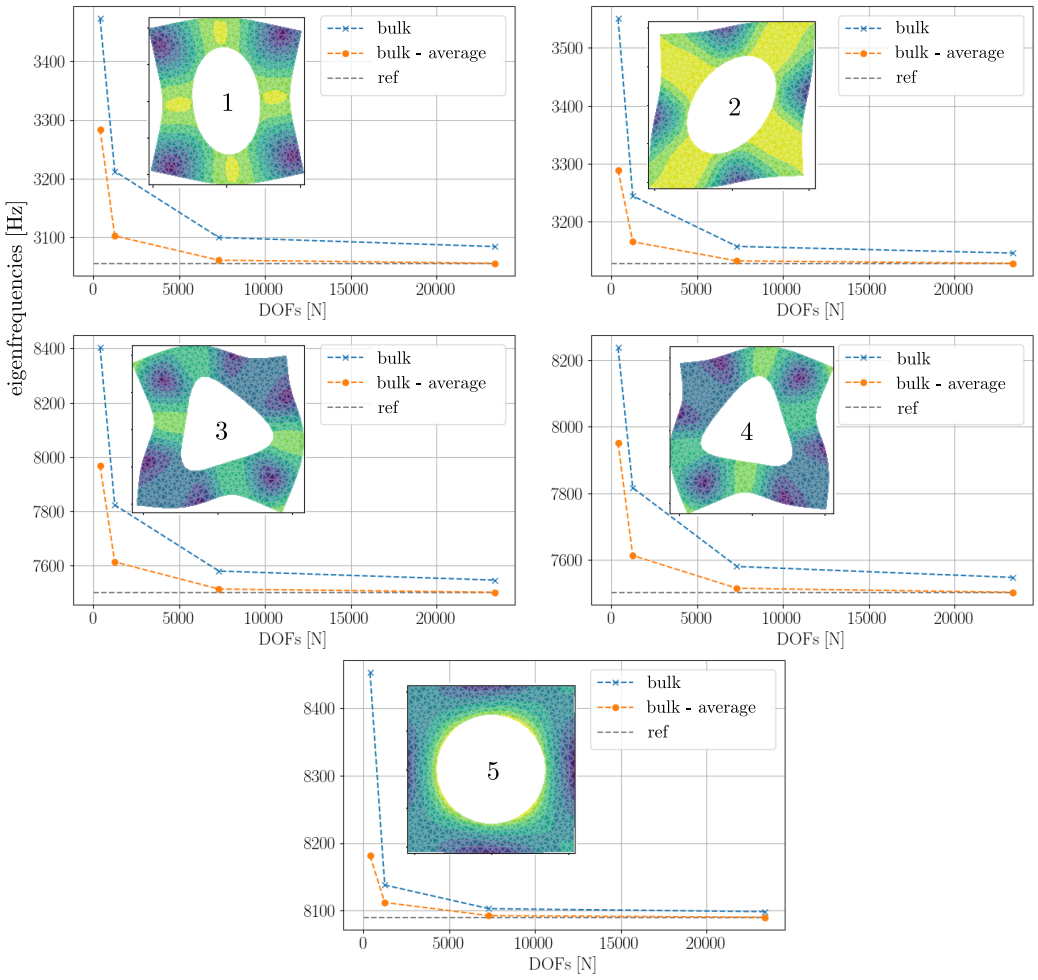

Figure 2.4: First five deformable eigenshapes close to zero of the RVEs and their convergence for different values of mesh resolution. Only bulk form with average-based smoothing is shown. The edge- and average- based smoothing relative difference is 0.0001%.

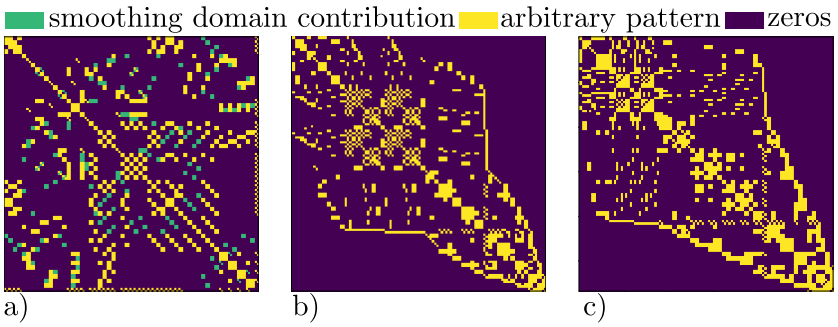

Figure 2.5: Sparsity patterns for standard FEM and edge smoothed: (**a**)comparison of initial sparsity patterns, (**b**) optimised sparsity pattern of standard FE method, and (**c**) optimised sparsity pattern of ES-FEM (reverse Cuthill–Mckee algorithm is used to optimise the sparsity patterns [29]). The number of non-zero entries within ES-FEM is $\sim 1.3\times$ higher the number of non-zero entries in the standard FE method.

Chapter 3

Individual Yarn Fibre Extraction from Micro-Computer Tomography: A Multilevel Machine Learning Approach

3.1 Introduction

Extracting the geometrical and topological features of complex fibrous structures, e.g. yarn, from micro-structural tomographic data is challenging. Hence, understanding the internal structure of yarn is a crucial step for determining how macro-mechanical parameters are influenced by inter-fibre mechanics and other physical effects. Using an adequately defined micro-structural model of yarn, a computational model can be established to find out the yarn micro-mechanics concerning full-resolution models [16, 73] or more efficient multi-scale models [101, 114, 102]. Nevertheless, prior to any computational modelling, an accurate geometry representation of the yarn structure must be provided. A few studies have focused on the tracing the individual fibres. Geisselmann et al. used a combination of the distance transform and skeletonisation methods to separate fibres individually. However, owing to noise and irregularity in the three-dimensional (3D) data, the fibres might not be continuous and the skeletonisation algorithm may generate the so-called 'H' connectivity (Figure 3.1) [26, 27]. The challenging step is to properly connect the disconnected part to obtain the original fibres. Hence, a suitable criterion must be met to connect the appropriate segments.

Geiselmann et al. proposed the use of stochastic models wherein the angle and length of the interconnecting segment were utilised to control the actual connection probability [26, 27]. Hu et al. used a multilevel tracing algorithm that simplified the decision criteria of pair selection [41]. Another method, which enjoys the benefits of popular geometrical structures (e.g. cylindrical structures), employed the Hessian eigenvalues to extract fibres [99]. Jerome et al. proposed another skeleton-based method suitable for low-density materials [67]. Viguié et al. used a local orientation map combined with dilatation operations to extract fibres and their contacts [103]. This chapter aims to describe the novel method for extracting the geometrical data of microCT scanned fibre like structures. The following challenges are introduced and part of them solved in next section. The fibre like structures in micro-CT posses several challenges for segmentation algorithms:

- random orientation and length of fibres
- severally overlapped fibres
- spatially inhomogeneous cross-section

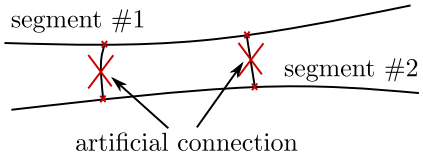

Figure 3.1: H-type connection occurring during skeletonisation of a noisy structure.

Although fibre-like structures are specific structures from the perspective of segmentation algorithms, geometrical extraction can be significantly simplified by reusing several specific properties provided by a certain fibre model. The simplest extraction can be observed in long and almost homogeneously oriented fibres. This is the case of a wide range of composite fibres and algorithms used the regularity and strength fibre assumption were proposed (a more enhanced approach has been presented in previous research [18]). The strength fibres allow us to extract centres from individual computer tomography (CT) stack cross sections by employing regular Hough-like methods. However, even in these simple cases, the computational cost can be minimised and more effective methods should be explored. Most algorithms use at least the basic morphological methods to extract useful information from 3D images. A very effective combination can be observed when the distance map and skeletonisation are used to extract the fibre centres [27]. Highly

enhanced methods, e.g. Hessian eigenvalues-based method, can be used for further extraction of structure-based information [99]. Herein, we propose a new method based on an efficient combination of regular 3D image analysis and a machine learning technique to efficiently extract individual fibres from micro-CT data.

3.2 Materials and Methods

The general workflow of image analysis on CT data is illustrated in Figure 3.2. The analysis involves optimal de-noising of raw data up to the final step that involves resampling and accurate tracking of fibre segments. The detailed steps are discussed in the following subsections.

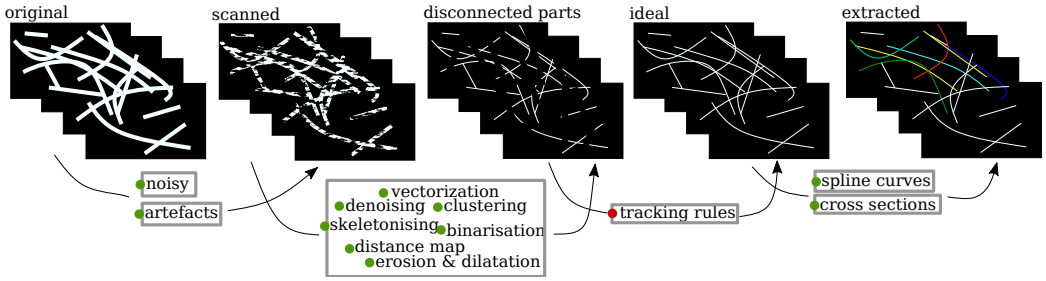

Figure 3.2: Workflow of fibre extraction from micro-CT data.

3.2.1 Fibre-like Structures

The tested fibre structures are planar textile labelled as **TEX-2DW** and yarn labelled as **TEX-Y**. The planar structure is made of polyamide material with a density of 420 [tex] and a thread count of 16/22 [1/cm]. Meanwhile, the yarn structure is made of polyester with a fibre diameter of ∼12 μm, package diameter of ∼131 μm and density of 25 [tex]. Both structures are presented in Figure 3.3. These images show an array with orthogonal indices wherein each member represents a grey value in the range 0–255. An example of raw grey-structure slices is shown in Figure 3.4.

3.2.2 Scanner Settings

The micro-CT scanner Rigaku nano3DX was used with a tube voltage ranging from 20 to 50 kV and a current up to 30 mA. The data array size of **TEX-Y** is $1427 \times 1442 \times 1250$ with a voxel spacing of 0.528 μm $\times$ 0.528 μm

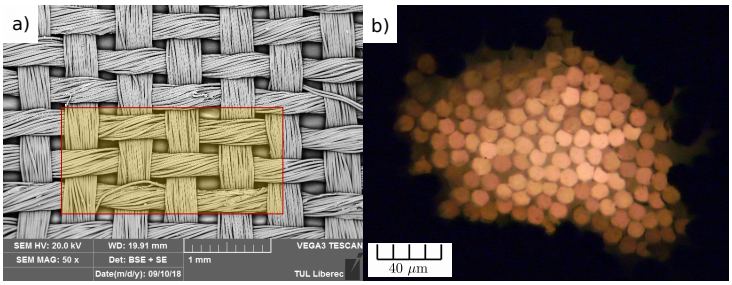

Figure 3.3: Electron microscopy slice of the woven structure **TEX-2DW** in which the region of interest (yellow window) is used for 3D scanning (a). A slice cut of yarn **TEX-Y** with visible cross sections of the individual fibre obtained using light microscopy.

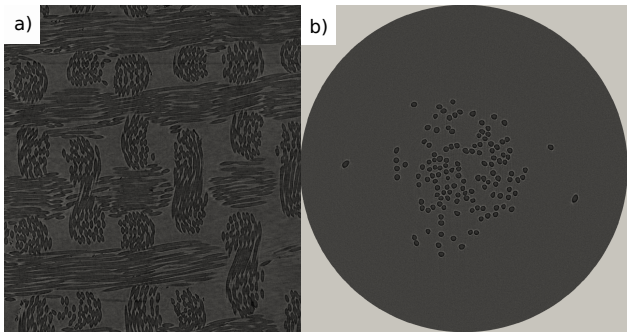

Figure 3.4: Grey z-slice example of **TEX-2DW** (a) and **TEX-Y** (b).

$\times$ 0.528 μm. Meanwhile, the data array size of **TEX-2DW** is 204$\times$1201$\times$551 with a voxel resolution of 1 μm $\times$ 1 μm $\times$ 1 μm.

3.2.3 Image Preprocessing

First, the stacks of the resultant CT were converted to a 3D array and the histogram was equalised. Second, the noise was removed using a median filter with a spherical structure element. Third, binarisation based on the threshold and Otsu's method was performed. After obtaining the binary structure, the Euclidean distance map was computed. Euclidean distance benefits from the circular cross section of individual fibres. Thus, at the fibre centre, the distance is minimal with respect to the background and peak occurs. Optimally, the peak has a value that is half of the fibre diameter. However, owing to uncertain observation, the peak filter works in the range 4.7–6.3 μm for **TEX-Y** and in the range 4.5–7 μm for woven **TEX-2DW**. The fibre diameter is provided by the manufacturer (see subsection 3.2.1) or

can be estimated from the distance map histogram. Moreover, the crossing fibres can be separated by the distance peaks; thus, no additional step is required (Figure 3.5). The new binarised data were obtained from the filter of the distance peaks based on the previously mentioned range. The morphological dilatation with a small structuring element was used to close the small gaps in the peaks. Finally, skeletonisation was applied on the binary array and one-pixel centres of the fibre parts were obtained. To remove 'H'-like connections and other crossings, the pixel was tested by 26 connectivity for the neighbourhoods and pixels with more than two neighbourhoods were removed. Thus, the disconnected parts were labelled and sorted in ascending order based on the length of the fibre parts.

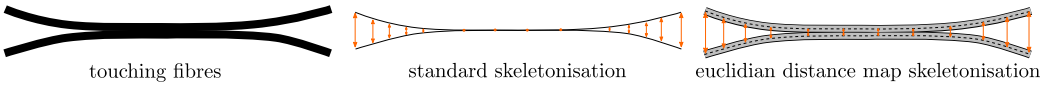

Figure 3.5: Regular skeletonisation issue (middle) with two fibres (left). The distance map disconnecting two fibres.

3.2.4 Vectorisation

For further work with disconnected discrete part of the fibres, the transformation into continuous representation is useful. We called the disconnected parts of the fibres 'segments', and each segment represented by a structure containing an unsorted pixel number but with identified ends is approximated by the b-spline curve (Figure 3.6). After the two candidates to be merged are identified, the b-spline curve is also used to connect them by approximating the missing coordinates between the candidates. The spline approximation quality is carefully investigated using the weighted squared residuals (Table 3.1) dependent on the smoothing factor s. The smoothing factor influences a compromise of the accuracy between interpolation and smoothness. The smoothing parameter in the range 0.01–0.05 often provides good results with respect to accuracy and smoothness. The spline is of the cubic order, and the first and second derivatives are used to determine the tangents and fibre curvatures, respectively. Moreover, each segment structure involves the evaluation method of the spline, control points, knots, residuals, end tangents and curvatures. Additional details on spline interpolation construction are described in [46].

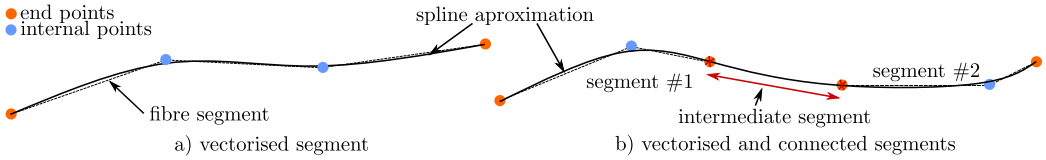

Figure 3.6: Fibre segment with cubic spline approximation (a). Merging of the two segments using the spline curve with smooth transition (b).

Table 3.1: Weighted squared sum of the residuals of the b-spline interpolation for various smoothing parameters s and both tested models.

residuals		
TEX-2DW	**TEX-Y**	s
1^{-7}	2^{-8}	0
5^{-4}	1^{-5}	0.1
3^{-2}	7^{-2}	1
6^{-1}	9^{-1}	10
6.25	8.13	100

3.2.5 Fibre Tracking

The fibres are disconnected and presented by segments. The manner of connecting the segments to obtain the original fibre is inspired from the work of Geiselmann [27, 26] (see Figure 3.7). Consider two segments: i and j. Each segment contains two end points that can be potentially connected to the other end points of another segment. We are looking for the potential pair described by inter-segments with length l_{ij}. With an inter-segment defined as a simple line joining the ends of the segments, we test a potential pair by verifying whether the inter-segments belong to a certain cone defined by the angles α_{ij} and α_{ji}. The angles are measured between the inter-segment and end tangents of the segments. By introducing the weighting factor w_r and maximal values l_{max} and α_{max}, we can the criterion function as the weighted sum of normalised partial members can be expressed as follows:

$$c_{ij} = (1 - w_r)\frac{l_{ij}}{l_{max}} + w_r\frac{\alpha_{ij} + \alpha_{ji}}{\alpha_{max}} < 1 \tag{3.1}$$

Every segment pair satisfying the above criterion is regarded as a potential candidate. The final pair is selected according to the smallest c_{ij} value and must pass the quality selection defined in the following section. Increasing the maximal distance between the fibre ends leads to a decrease in maximal angles (but still depends on the measured angles α_{ij} and α_{ji}). Thus, the geometrical relation is clear [27]. However, we will not use this relation for

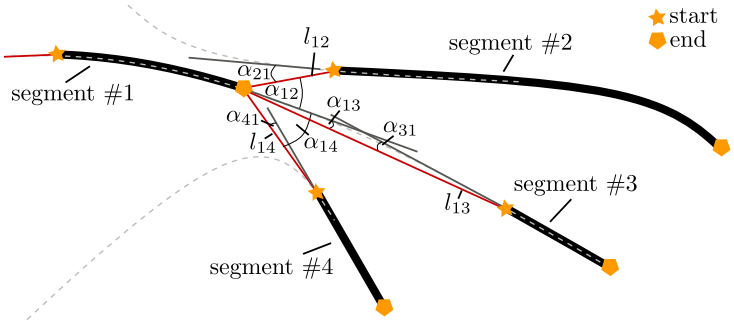

Figure 3.7: Example of the distance and angle measurement between potential candidates for pairing.

the criterion. Instead, we will maintain them separately. Various connectivity scenarios are shown in Figure 3.8. The optimal values of parameters $\alpha_{ij}, \alpha_{ji}, l_{ij}$ as well the directions of similar segment ends should be as small as possible. Nevertheless, if the fibre ends are close and slightly excentered, then the angles can be close to 90° with a decrease in distance. After performing the tracking, the results were evaluated. The new spline curve of the inter-segment was discretised onto the original CT data space and dilated with a small structuring element sphere. The mean of the grey values corresponding to the inter-segment spline was used as the quality evaluator. When determining whether the given inter-segment is correctly identified, the Gaussian mixture cluster classifier was trained on the original CT data [84].

3.2.6 Algorithms and Implementation Details

Image algorithms often work with large data collections, and they are even a highly demanding issue in 3D. In the proposed algorithms shown in Figure 3.9, the main steps required for the effective segmentation of fibres are introduced. The input required by the algorithm is composed of the distance map field and raw CT data. Both arrays are encoded in hdf5 format [24] with uint8/float64 data type. Vectorisation is one of the most computationally intensive tasks because it requires to implement filtering, binarisation, skeletonisation and segment separation. After obtaining the initial segments, they are resampled to have a consistent resolution. The initial control parameters are set by the user and are defined by following Python dictionary.

- "l_{max}": [...,...,...] is a list of maximal distance parameters
- "α_{max}": [...,...,...] is a list of alpha angles

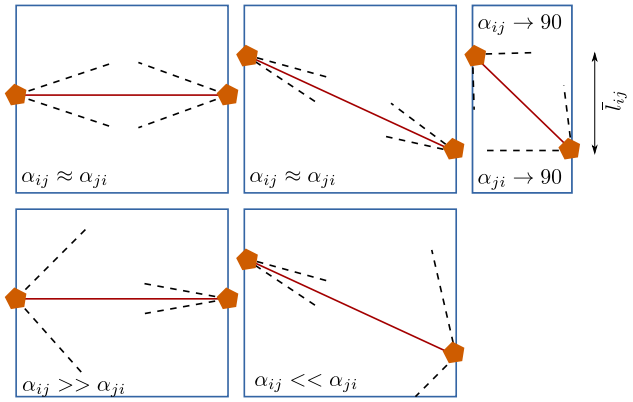

Figure 3.8: Different fibre connection scenarios. The angles are measured from both sides depending on the fibre orientation. Dotted line expresses the fibre end direction. Orange line expresses the inter-fibre segment. The angle α_{ij} is approaching 90 °when the projected inter-fibre length $\bar{l}_{ij}$ goes to inter-fibre length l_{ij}.

- "w_r": [...,...,...] is a list of weighting constants

The parameters are referenced to the previous sections to mainly discuss the algorithm. Now, a segment is represented by an object that allows for recursive merging of segments and respecting the parent–child relationship. Given that the segment connectivity is defined by the spatial coordinates of the segment end points, the binary search graph (Kd tree) is constructed before the main loop starts. At the current point, the pairing of the segments runs on two queues: **finished** and **unfinished**. Once a pair of two matching segments is obtained, these segments are merged and the partial segments are dropped out from the **unfinished** queue and the new segment is pushed to the **finished** queue. Once the **unfinished** queue is empty, the resultant segments are further evaluated. If necessary, the matching criteria can be adapted and the new level can continue. The main code is developed in Python language, with the critical parts (e.g. graph construction, searching, merging and b-spline interpolation) written in C++. The code is written in an objective manner.

3.3 Results

The model parameters l_{max}, α_{max} and w_r are experimentally estimated based on the parametric approach and careful investigation of the initial and level-based potentially matched pair of segments. The mean values of the grey data

initialise distance map and raw data
vectorise
resample and sort initial segments
set the initial control parameters

[FOR] **levels**

- compute graph search tree
- [WHILE] **unfinished**
  - get actual segment
  - match segment according to control parameters
  - merge segments
  - drop it out from **unfinished** queue and put to **finished objects**
- evaluate global properties
- adapt global criteria and filter new segments
- put all **finished** segments to **unfinished**

Figure 3.9: Algorithm scheme of fibre segmentation.

for both models were estimated by Gaussian mixed clustering. The clusters corresponding to the fibre structure were identified as follows: mean value of 90 and variance of ± 61 for **TEX-2DW**, whereas mean value of 198 and variance of ± 51 for **TEX-Y** (see Figure 3.10). The trained classifier is used to decide whether the newly created segment corresponds to the grey values. The pairs that did not pass the quality criteria are excluded. The optimal model parameters are defined in Table 3.2. To decide whether to start a new level, the algorithm verifies the number of new pairs for the previous control parameter set. If the result is non-zero, then it continues to another level using the same parameters. Meanwhile, if the number of new pairs is zero, then the algorithm increases the control parameters and starts a new pairing level. In addition, the control parameters can be interactively manipulated but are not efficient. However, in several cases, manual correction may be required or the weighting parameter w_r can be corrected to obtain more fine control. The segmentation results of **TEX-Y** are shown in Figure 3.11. The main characteristics, i.e. fibre diameter and length, are spatially shown in Figure 3.12. With the given level-controlled parameters, the resultant fibres

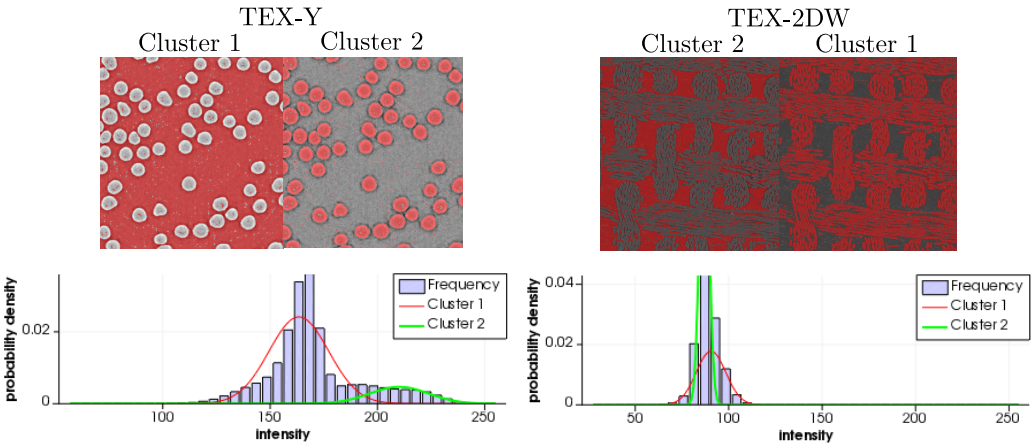

Figure 3.10: Gaussian mixture cluster classification [84, 113] for woven fabric and yarn CT data. Two clusters of grey values are identified. The red part corresponds to a mask of clustered data. The decision accuracy of the trained cluster classification is evaluated via a cross-validation test/trained threefold testing scheme with the resultant prediction accuracy within the range 81–97% [84].

Table 3.2: Optimal control parameters and number of levels for both models. The weighting parameter w_r is set to 0.5. A couple of numbers are present: the first one is l_{max} [mm], whereas the second one is α_{max} [°].

TEX-2DW	0.01, 10	0.01, 10	0.03, 30	0.03, 30	0.05, 40	0.08, 40	0.1, 40
TEX-Y	0.01, 50	0.01, 50	0.01, 50	0.015, 50	0.015, 50		

are correctly identified with 100% success. In total, 136 fibres are present. The mean length of the fibre is 0.734 mm, and the diameter is 0.0051 mm. The initial number of the fibres and their length are shown at the upper right-hand side of the images in Figure 3.11. Owing to a large number of fibre parts, the length distribution is significantly changed to lower values (mean: 0.33) with high variance scatter (0.21). The results of fibre extraction for highly noisy (and lower contrast - Figure 3.10) and corrupted (inter-fibre impurity) CT data for the **TEX-2DW** model are shown in Figure 3.13. Meanwhile, the fibre length distribution is shown in Figure 3.12. Owing to the two orthogonal directions of fibre bundles, one family of fibres has a mean length of 0.783 mm with a perpendicularity of 1.253 mm. However, only 63% of the fibres was correctly identified (at total of 255 fibres are present based on the careful observation of the CT data). This was caused by large corrupted parts, where uniquely guessing the pairs using a deterministic approach is not possible. Further, the fibre mean radius of **TEX-2DW** was 0.0057 mm.

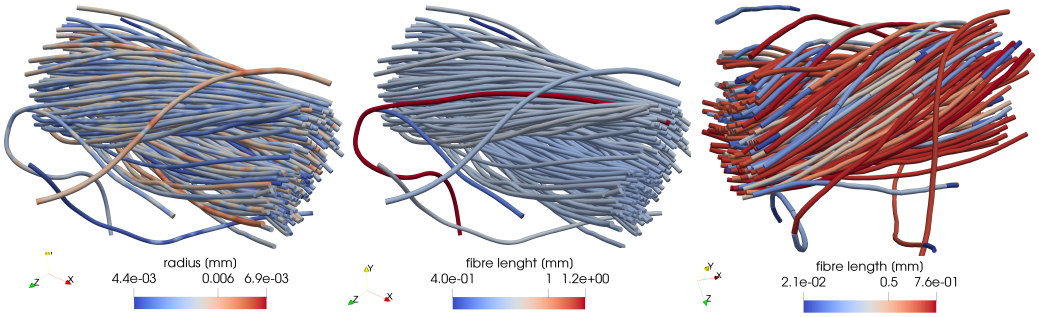

Figure 3.11: Segmented yarn with 100% success in all available fibres (left and middle). The right picture contains the initial distribution length of the fibres.

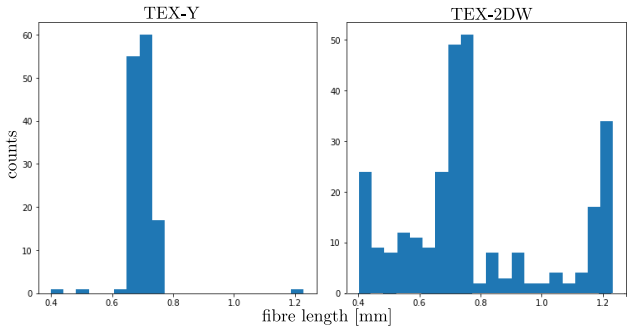

Figure 3.12: Final length distribution for both models.

3.4 Discussion

Developing complex and physically relevant models establishes a significant interest in scientific community. Fibre-like structures are observed in many material structures, and inspection of their physics is an important task. CT can provide an important view of fibre structures, often more than the requirements, particularly in computational models, wherein the geometry becomes the focus. Owing to the complexity of fibre structures with many contact bonds and overlapping parts, accurate individual fibre identification is a challenging task. Although a few studies have focused on fibre extraction, a consistent family of methods is not well developed. We propose a simple extraction algorithm connected with standard morphological operations to extract individual fibres from the CT data with sufficient accuracy and speed.

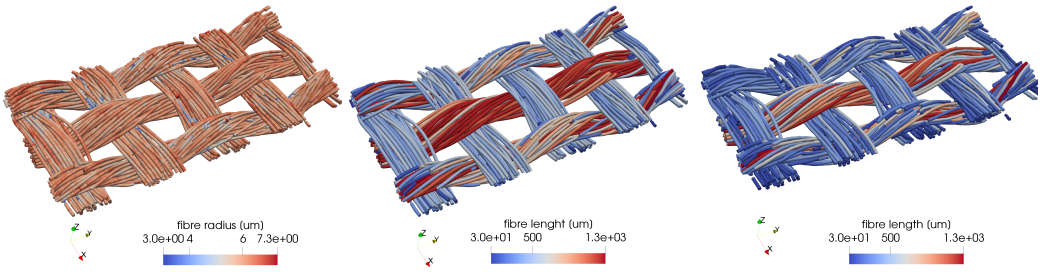

Figure 3.13: Extracted woven fibres and their properties obtained from highly noisy and corrupted micro-CT data: (middle) final fibre length distribution; (right) initial fibre length distribution.

The algorithm relies on the multilevel strategy, where at each level, a pair of fibres is searched to ensure that it matches with the given control criteria and quality. Using a multilevel strategy allows us to adaptively change the criteria and fine tune the results. This advantage is one of the main differences that is not observed in the multilevel strategy used in a previous study [41]. The extraction quality can be further influenced by practical use of morphological operations and more advanced filtering techniques. Nevertheless, the most critical part is to obtain a sufficient quality of CT data. This is apparent in our results. The individual yarn model **TEX-Y** proceeded with 100% accuracy. All fibres were properly separated, and the fibre diameter was accurately identified. As a demonstration, the second model of the woven fabric with low data contrast corrupted by noise, referred to as **TEX-2DW**, was correctly identified only at 63% with respect to the total number of fibres.

The computational sources necessary for fibre segmentation are relatively low (136 and 186 fibres identified in 2 and 5 s, respectively) in comparison with those required by the stochastic algorithm (83 min for 903 fibres) proposed in previous research [27]. However, these sources may depend on fibre structure complexity and segment end proximity. The critical part is the quick nearest neighbour lookup, which should be efficiently implemented by constructing an optimal graph, e.g. a Kd tree algorithm [68]. The initial raw data, e.g. Euclidean distance field or field from skeletonisation algorithm, required as the input are already implemented in an efficient way in library [46]. Processing these data do not usually pose performance bottlenecks.

Evidently, the proposed algorithm can be improved in control parameter evaluation. The current model relies on the simple deterministic criteria, which commonly need a user initial setup and can be adapted during level iteration owing to the multilevel approach. Nevertheless, the unique decision

regarding the best suited segment pair is not always detectable (particularly in the case of noisy CT data), and hence, mismatches occur. Although mismatches are detected by evaluating the newly created segment, which may lead to this segment deletion, still, several mismatched segments propagate up to the end of level iteration or some potentially connectible segments with long proximity are not accurately detected. Thus, using more advanced criteria can aid in improving decision sensitivity and should be supported by the probabilistic approach proposed in previous research [27] or by some other approaches, e.g. machine learning classifiers or Fuzzy logic [111].

Bibliography

[1] Amos Alexander and Jerome T Tzeng. Three dimensional effective properties of composite materials for finite element applications. *Journal of composite materials*, 31(5):466–485, 1997.

[2] Patrick R Amestoy, Iain S Duff, Jean-Yves L'Excellent, and Jacko Koster. A fully asynchronous multifrontal solver using distributed dynamic scheduling. *SIAM Journal on Matrix Analysis and Applications*, 23(1):15–41, 2001.

[3] Erik Andreassen and Casper Schousboe Andreasen. How to determine composite material properties using numerical homogenization. *Computational Materials Science*, 83:488–495, 2014.

[4] Chandrasekhar Annavarapu. *An efficient finite element method for interface problems*. PhD thesis, Duke University, 2013.

[5] Satish Balay, Shrirang Abhyankar, Mark Adams, Peter Brune, Kris Buschelman, L Dalcin, W Gropp, Barry Smith, D Karpeyev, Dinesh Kaushik, et al. Petsc users manual revision 3.7. Technical report, Argonne National Lab.(ANL), Argonne, IL (United States), 2016.

[6] Manik Bansal, IV Singh, BK Mishra, and SPA Bordas. A parallel and efficient multi-split xfem for 3-d analysis of heterogeneous materials. *Computer Methods in Applied Mechanics and Engineering*, 347:365–401, 2019.

[7] Manik Bansal, IV Singh, RU Patil, Susanne Claus, and SPA Bordas. A simple and robust computational homogenization approach for heterogeneous particulate composites. *Computer Methods in Applied Mechanics and Engineering*, 2019.

[8] Alain Bensoussan, Jacques-Louis Lions, and George Papanicolaou. *Asymptotic analysis for periodic structures*, volume 374. American Mathematical Soc., 2011.

[9] Ericka Brivadis, Annalisa Buffa, Barbara Wohlmuth, and Linus Wunderlich. Isogeometric mortar methods. *Computer Methods in Applied Mechanics and Engineering*, 284:292–319, 2015.

[10] Louise P Brown and Martin Sherburn. louisepb/texgen: Texgen v3.10.0, December 2017. This software is currently funded by EPSRC Research Software Engineering Fellowship - Software for Textile Modelling and Simulation, EP/N019040/1.

[11] Erik Burman, Susanne Claus, Peter Hansbo, Mats G Larson, and André Massing. Cutfem: Discretizing geometry and partial differential equations. *International Journal for Numerical Methods in Engineering*, 104(7):472–501, 2015.

[12] Jiun-Shyan Chen, Cheng-Tang Wu, Sangpil Yoon, and Yang You. A stabilized conforming nodal integration for galerkin mesh-free methods. *International Journal for Numerical Methods in Engineering*, 50(2):435–466.

[13] Franz Chouly, Patrick Hild, and Yves Renard. Symmetric and non-symmetric variants of nitsche's method for contact problems in elasticity: theory and numerical experiments. *Mathematics of Computation*, 84(293):1089–1112, 2015.

[14] Fabien Cornaton, Pierre Perrochet, and Hans-Jörg Diersch. A finite element formulation of the outlet gradient boundary condition for convective–diffusive transport problems. *International journal for numerical methods in engineering*, 61(15):2716–2732, 2004.

[15] Liang Cui and Catherine O'Sullivan. Analysis of a triangulation based approach for specimen generation for discrete element simulations. *Granular Matter*, 5(3):135–145, 2003.

[16] Damien Durville. Finite element simulation of textile materials at the fiber scale. *arXiv preprint arXiv:0912.1268*, 2009.

[17] Anand Embar, John Dolbow, and Isaac Harari. Imposing dirichlet boundary conditions with nitsche's method and spline-based finite elements. *International journal for numerical methods in engineering*, 83(7):877–898, 2010.

[18] Monica J. Emerson, Kristine M. Jespersen, Anders B. Dahl, Knut Conradsen, and Lars P. Mikkelsen. Individual fibre segmentation from 3d x-ray computed tomography for characterising the fibre orientation in

unidirectional composite materials. *Composites Part A: Applied Science and Manufacturing*, 97:83 – 92, 2017.

[19] Robert D Falgout and Ulrike Meier Yang. hypre: A library of high performance preconditioners. In *International Conference on Computational Science*, pages 632–641. Springer, 2002.

[20] Philipp Farah, Alexander Popp, and Wolfgang A. Wall. Segment-based vs. element-based integration for mortar methods in computational contact mechanics. *Computational Mechanics*, 55(1):209–228, Jan 2015.

[21] Kathrin A Fischer and Peter Wriggers. Mortar based frictional contact formulation for higher order interpolations using the moving friction cone. *Computer methods in applied mechanics and engineering*, 195(37):5020–5036, 2006.

[22] B Flemisch, MA Puso, and BI Wohlmuth. A new dual mortar method for curved interfaces: 2d elasticity. *International journal for numerical methods in engineering*, 63(6):813–832, 2005.

[23] James D Foley, Foley Dan Van, Andries Van Dam, Steven K Feiner, John F Hughes, J HUGHES, and EDWARD ANGEL. *Computer graphics: principles and practice*, volume 12110. Addison-Wesley Professional, 1996.

[24] Mike Folk, Gerd Heber, Quincey Koziol, Elena Pourmal, and Dana Robinson. An overview of the hdf5 technology suite and its applications. In *Proceedings of the EDBT/ICDT 2011 Workshop on Array Databases*, pages 36–47. ACM, 2011.

[25] D Fujii, BC Chen, and Noboru Kikuchi. Composite material design of two-dimensional structures using the homogenization design method. *International Journal for Numerical Methods in Engineering*, 50(9):2031–2051, 2001.

[26] Gerd Gaiselmann, Dieter Froning, Christian Tötzke, Christian Quick, Ingo Manke, Werner Lehnert, and Volker Schmidt. Stochastic 3d modeling of non-woven materials with wet-proofing agent. *International Journal of Hydrogen Energy*, 38(20):8448–8460, 2013.

[27] Gerd Gaiselmann, Ingo Manke, Werner Lehnert, and Volker Schmidt. Extraction of curved fibers from 3d data. In *Forum Bildverarbeitung 2012*, page 119. KIT Scientific Publishing, 2012.

[28] M.G.D. Geers, V.G. Kouznetsova, and W.A.M. Brekelmans. Multi-scale computational homogenization: Trends and challenges. *Journal of Computational and Applied Mathematics*, 234(7):2175 – 2182, 2010. Fourth International Conference on Advanced COmputational Methods in ENgineering (ACOMEN 2008).

[29] Norman E Gibbs, William G Poole, Jr, and Paul K Stockmeyer. An algorithm for reducing the bandwidth and profile of a sparse matrix. *SIAM Journal on Numerical Analysis*, 13(2):236–250, 1976.

[30] William Gropp, Ewing Lusk, and Anthony Skjellum. *Using MPI: portable parallel programming with the message-passing interface*, volume 1. MIT press, 1999.

[31] JoséMiranda Guedes and Noboru Kikuchi. Preprocessing and postprocessing for materials based on the homogenization method with adaptive finite element methods. *Computer methods in applied mechanics and engineering*, 83(2):143–198, 1990.

[32] Peter Hansbo. Nitsche's method for interface problems in computational mechanics. *GAMM-Mitteilungen*, 28(2):183–206, 2005.

[33] S Hartmann, S Brunssen, E Ramm, and B Wohlmuth. Unilateral nonlinear dynamic contact of thin-walled structures using a primal-dual active set strategy. *International journal for numerical methods in engineering*, 70(8):883–912, 2007.

[34] Zvi Hashin and Shmuel Shtrikman. A variational approach to the theory of the elastic behaviour of multiphase materials. *Journal of the Mechanics and Physics of Solids*, 11(2):127–140, 1963.

[35] ZC He, GY Li, ZH Zhong, AG Cheng, GY Zhang, Eric Li, and GR Liu. An es-fem for accurate analysis of 3d mid-frequency acoustics using tetrahedron mesh. *Computers & Structures*, 106:125–134, 2012.

[36] ZC He, GY Li, ZH Zhong, AG Cheng, GY Zhang, GR Liu, Eric Li, and Z Zhou. An edge-based smoothed tetrahedron finite element method (es-t-fem) for 3d static and dynamic problems. *Computational mechanics*, 52(1):221–236, 2013.

[37] ZC He, GR Liu, ZH Zhong, SC Wu, GY Zhang, and AG Cheng. An edge-based smoothed finite element method (es-fem) for analyzing three-dimensional acoustic problems. *Computer Methods in Applied Mechanics and Engineering*, 199(1-4):20–33, 2009.

[38] Vicente Hernandez, Jose E Roman, and Vicente Vidal. Slepc: A scalable and flexible toolkit for the solution of eigenvalue problems. *ACM Transactions on Mathematical Software (TOMS)*, 31(3):351–362, 2005.

[39] J.A. Hernández, J. Oliver, A.E. Huespe, M.A. Caicedo, and J.C. Cante. High-performance model reduction techniques in computational multiscale homogenization. *Computer Methods in Applied Mechanics and Engineering*, 276:149 – 189, 2014.

[40] Scott J Hollister and Noboru Kikuchi. A comparison of homogenization and standard mechanics analyses for periodic porous composites. *Computational Mechanics*, 10(2):73–95, 1992.

[41] Xiang Huang, Donghui Wen, Yanwei Zhao, Qinghui Wang, Wei Zhou, and Daxiang Deng. Skeleton-based tracing of curved fibers from 3d x-ray microtomographic imaging. *Results in physics*, 6:170–177, 2016.

[42] Stefan Jacques, Ives De Baere, and Wim Van Paepegem. Application of periodic boundary conditions on multiple part finite element meshes for the meso-scale homogenization of textile fabric composites. *Composites Science and Technology*, 92:41–54, 2014.

[43] Yunyao Jiang and Yaning Li. 3d printed auxetic mechanical metamaterial with chiral cells and re-entrant cores. *Scientific reports*, 8(1):2397, 2018.

[44] August Johansson and Mats G Larson. A high order discontinuous galerkin nitsche method for elliptic problems with fictitious boundary. *Numerische Mathematik*, 123(4):607–628, 2013.

[45] Eric Jones, Travis Oliphant, and Pearu Peterson. {SciPy}: open source scientific tools for {Python}. 2014.

[46] Eric Jones, Travis Oliphant, Pearu Peterson, et al. SciPy: Open source scientific tools for Python, 2001–. [Online; accessed ¡today¿].

[47] Ruben Juanes, Javier Samper, and Jorge Molinero. A general and efficient formulation of fractures and boundary conditions in the finite element method. *International Journal for Numerical Methods in Engineering*, 54(12):1751–1774.

[48] Ruben Juanes, Javier Samper, and Jorge Molinero. A general and efficient formulation of fractures and boundary conditions in the finite element method. *International Journal for Numerical Methods in Engineering*, 54(12):1751–1774, 2002.

[49] Mika Juntunen and Rolf Stenberg. Nitsche's method for general boundary conditions. *Mathematics of computation*, 78(267):1353–1374, 2009.

[50] T. Kanit, S. Forest, I. Galliet, V. Mounoury, and D. Jeulin. Determination of the size of the representative volume element for random composites: statistical and numerical approach. *International Journal of Solids and Structures*, 40(13):3647 – 3679, 2003.

[51] Ravi Kiran and Kapil Khandelwal. Complex step derivative approximation for numerical evaluation of tangent moduli. *Computers & Structures*, 140(Supplement C):1 – 13, 2014.

[52] V Kouznetsova, WAM Brekelmans, and FPT Baaijens. An approach to micro-macro modeling of heterogeneous materials. *Computational Mechanics*, 27(1):37–48, 2001.

[53] VG Varvara Kouznetsova. *Computational homogenization for the multi-scale analysis of multi-phase materials*. PhD thesis, Technische Universiteit Eindhoven, 2002.

[54] Bishnu P Lamichhane and Barbara I Wohlmuth. Mortar finite elements for interface problems. *Computing*, 72(3-4):333–348, 2004.

[55] Fredrik Larsson, Kenneth Runesson, and Fang Su. Variationally consistent computational homogenization of transient heat flow. *International Journal for Numerical Methods in Engineering*, 81(13):1659–1686, 2010.

[56] Ilya Lashuk, Merico Argentati, Evgueni Ovtchinnikov, and Andrew Knyazev. Preconditioned eigensolver lobpcg in hypre and petsc. In *Domain decomposition methods in science and engineering XVI*, pages 635–642. Springer, 2007.

[57] Eric Yiming Li, Zhongpu Zhang, C Chang, G. Liu, and Qi Li. Homogenization for composite material properties using smoothed finite element method. 2014.

[58] Jian Li, Viacheslav Slesarenko, and Stephan Rudykh. Auxetic multiphase soft composite material design through instabilities with application for acoustic metamaterials. *Soft Matter*, 14:6171–6180, 2018.

[59] Chenchen Liu and Celia Reina. Discrete averaging relations for micro to macro transition. *Journal of Applied Mechanics*, 83(8):081006, 2016.

[60] GR Liu, KY Dai, and THOI T Nguyen. A smoothed finite element method for mechanics problems. *Computational Mechanics*, 39(6):859–877, 2007.

[61] GR Liu, TT Nguyen, KY Dai, and KY Lam. Theoretical aspects of the smoothed finite element method (sfem). *International journal for numerical methods in Engineering*, 71(8):902–930, 2007.

[62] GR Liu, T Nguyen-Thoi, and KY Lam. An edge-based smoothed finite element method (es-fem) for static, free and forced vibration analyses of solids. *Journal of Sound and Vibration*, 320(4-5):1100–1130, 2009.

[63] GR Liu, T Nguyen-Thoi, Hb Nguyen-Xuan, and KY Lam. A node-based smoothed finite element method (ns-fem) for upper bound solutions to solid mechanics problems. *Computers & structures*, 87(1-2):14–26, 2009.

[64] Gui-Rong Liu. *Mesh free methods: moving beyond the finite element method*. CRC press, 2002.

[65] Gui-Rong Liu and Nguyen Thoi Trung. *Smoothed finite element methods*. CRC press, 2016.

[66] Zeliang Liu, Mark Fleming, and Wing Kam Liu. Microstructural material database for self-consistent clustering analysis of elastoplastic strain softening materials. *Computer Methods in Applied Mechanics and Engineering*, 330:547 – 577, 2018.

[67] Jérôme Lux. Automatic segmentation and structural characterization of low density fibreboards. *Image Analysis & Stereology*, 32(1):13–25, 2013.

[68] Songrit Maneewongvatana and David M Mount. Analysis of approximate nearest neighbor searching with clustered point sets. *Data Structures, Near Neighbor Searches, and Methodology*, 59:105–123, 2002.

[69] André Massing, Mats G Larson, and Anders Logg. Efficient implementation of finite element methods on nonmatching and overlapping meshes in three dimensions. *SIAM Journal on Scientific Computing*, 35(1):C23–C47, 2013.

[70] Karel Matouš, Marc GD Geers, Varvara G Kouznetsova, and Andrew Gillman. A review of predictive nonlinear theories for multiscale modeling of heterogeneous materials. *Journal of Computational Physics*, 330:192–220, 2017.

[71] Jean-Claude Michel, Hervé Moulinec, and P Suquet. Effective properties of composite materials with periodic microstructure: a computational approach. *Computer methods in applied mechanics and engineering*, 172(1-4):109–143, 1999.

[72] Fanny Moravec and Sophie Roman. Numerical computing of elastic homogenized coefficients for periodic fibrous tissue. *Applied and Computational Mechanics*, 3:141–152, 2009.

[73] N. Naouar, E. Vidal-Sallé, J. Schneider, E. Maire, and P. Boisse. Meso-scale fe analyses of textile composite reinforcement deformation based on x-ray computed tomography. *Composite Structures*, 116:165 – 176, 2014.

[74] V-D Nguyen, Eric Béchet, Christophe Geuzaine, and Ludovic Noels. Imposing periodic boundary condition on arbitrary meshes by polynomial interpolation. *Computational Materials Science*, 55:390–406, 2012.

[75] Van-Dung Nguyen, Ling Wu, and Ludovic Noels. Unified treatment of microscopic boundary conditions and efficient algorithms for estimating tangent operators of the homogenized behavior in the computational homogenization method. *Computational Mechanics*, 59(3):483–505, Mar 2017.

[76] Vinh Phu Nguyen, Pierre Kerfriden, Marco Brino, Stéphane P. A. Bordas, and Elvio Bonisoli. Nitsche's method for two and three dimensional nurbs patch coupling. *Computational Mechanics*, 53(6):1163–1182, Jun 2014.

[77] Hung Nguyen-Xuan, Stéphane Bordas, and Hung Nguyen-Dang. Smooth finite element methods: convergence, accuracy and properties. *International Journal for Numerical Methods in Engineering*, 74(2):175–208, 2008.

[78] Vinh Phu Nguyena, Pierre Kerfriden, and Susanne Clausb Stephane Bordas. Nitsche's method method for mixed dimensional analysis: conforming and non-conforming continuum-beam and continuum-plate coupling. *arXiv preprint arXiv:1308.2910*, 2013.

[79] Stephen M Omohundro. *Five balltree construction algorithms*. International Computer Science Institute Berkeley, 1989.

[80] Ouail Ouchetto and Saad Zaamoun. Periodic boundary conditions in the fem using arbitrary meshes. In *Microwave, Radar and Wireless Communications (MIKON), 2016 21st International Conference on*, pages 1–3. IEEE, 2016.

[81] A.R. Owens, J. Kópházi, and M.D. Eaton. Optimal trace inequality constants for interior penalty discontinuous galerkin discretisations of elliptic operators using arbitrary elements with non-constant jacobians. *Journal of Computational Physics*, 350:847 – 870, 2017.

[82] I Özdemir, WAM Brekelmans, and Marc GD Geers. Fe2 computational homogenization for the thermo-mechanical analysis of heterogeneous solids. *Computer Methods in Applied Mechanics and Engineering*, 198(3-4):602–613, 2008.

[83] I Özdemir, WAM Brekelmans, and MGD Geers. Computational homogenization for heat conduction in heterogeneous solids. *International journal for numerical methods in engineering*, 73(2):185–204, 2008.

[84] F. Pedregosa, G. Varoquaux, A. Gramfort, V. Michel, B. Thirion, O. Grisel, M. Blondel, P. Prettenhofer, R. Weiss, V. Dubourg, J. Vanderplas, A. Passos, D. Cournapeau, M. Brucher, M. Perrot, and E. Duchesnay. Scikit-learn: Machine learning in Python. *Journal of Machine Learning Research*, 12:2825–2830, 2011.

[85] P Perrochet. Finite hyperelements: a 4d geometrical framework using covariant bases and metric tensors. *Communications in numerical methods in engineering*, 11(6):525–534, 1995.

[86] Alexander Popp, Markus Gitterle, Michael W Gee, and Wolfgang A Wall. A dual mortar approach for 3d finite deformation contact with consistent linearization. *International Journal for Numerical Methods in Engineering*, 83(11):1428–1465, 2010.

[87] Alexander Popp, Alexander Seitz, Michael W Gee, and Wolfgang A Wall. Improved robustness and consistency of 3d contact algorithms based on a dual mortar approach. *Computer Methods in Applied Mechanics and Engineering*, 264:67–80, 2013.

[88] Michael A Puso. A 3d mortar method for solid mechanics. *International Journal for Numerical Methods in Engineering*, 59(3):315–336, 2004.

[89] Michael A Puso, TA Laursen, and Jerome Solberg. A segment-to-segment mortar contact method for quadratic elements and large deformations. *Computer methods in applied mechanics and engineering*, 197(6-8):555–566, 2008.

[90] Michael A Puso and Tod A Laursen. Mesh tying on curved interfaces in 3d. *Engineering Computations*, 20(3):305–319, 2003.

[91] Romain Quey, Aurélien Villani, and Claire Maurice. Nearly uniform sampling of crystal orientations. *Journal of Applied Crystallography*, 51(4):1162–1173, Aug 2018.

[92] FJP Reis and FM Andrade Pires. A mortar based approach for the enforcement of periodic boundary conditions on arbitrarily generated meshes. *Computer Methods in Applied Mechanics and Engineering*, 274:168–191, 2014.

[93] F.J.P. Reis and F.M. Andrade Pires. A mortar based approach for the enforcement of periodic boundary conditions on arbitrarily generated meshes. *Computer Methods in Applied Mechanics and Engineering*, 274(Supplement C):168 – 191, 2014.

[94] Henning Richter. Mote3d: an open-source toolbox for modelling periodic random particulate microstructures. *Modelling and Simulation in Materials Science and Engineering*, 25(3):035011, 2017.

[95] Carl Sandstöm, Fredrik Larsson, and Kenneth Runesson. Weakly periodic boundary conditions for the homogenization of flow in porous media. *Advanced Modeling and Simulation in Engineering Sciences*, 1(1):1–24, 2014.

[96] I Temizer, P Wriggers, and TJR Hughes. Three-dimensional mortar-based frictional contact treatment in isogeometric analysis with nurbs. *Computer Methods in Applied Mechanics and Engineering*, 209:115–128, 2012.

[97] K Terada, T Ito, and N Kikuchi. Characterization of the mechanical behaviors of solid-fluid mixture by the homogenization method. *Computer methods in applied mechanics and engineering*, 153(3-4):223–257, 1998.

[98] Kenjiro Terada, Muneo Hori, Takashi Kyoya, and Noboru Kikuchi. Simulation of the multi-scale convergence in computational homogenization approaches. *International Journal of Solids and Structures*, 37(16):2285 – 2311, 2000.

[99] Matthias Teßmann, Stephan Mohr, Svitlana Gayetskyy, Ulf Haßler, Randolf Hanke, and Günther Greiner. Automatic determination of fiber-length distribution in composite material using 3d ct data. *EURASIP journal on advances in signal processing*, 2010(1):545030, 2010.

[100] J.M. Tyrus, M. Gosz, and E. DeSantiago. A local finite element implementation for imposing periodic boundary conditions on composite micromechanical models. *International Journal of Solids and Structures*, 44(9):2972 – 2989, 2007.

[101] Z. Ullah, Ł. Kaczmarczyk, S.A. Grammatikos, M.C. Evernden, and C.J. Pearce. Multi-scale computational homogenisation to predict the long-term durability of composite structures. *Computers and Structures*, 181:21 – 31, 2017. UK Association of Computational Mechanics.

[102] Andy Vanaerschot, Brian N. Cox, Stepan V. Lomov, and Dirk Vandepitte. Multi-scale modelling strategy for textile composites based on stochastic reinforcement geometry. *Computer Methods in Applied Mechanics and Engineering*, 310:906 – 934, 2016.

[103] J Viguié, P Latil, L Orgéas, PJJ Dumont, S Rolland du Roscoat, J-F Bloch, C Marulier, and O Guiraud. Finding fibres and their contacts within 3d images of disordered fibrous media. *Composites Science and Technology*, 89:202–210, 2013.

[104] Rongqiao Wang, Long Zhang, Dianyin Hu, Chunhui Liu, Xiuli Shen, Chongdu Cho, and Bo Li. A novel approach to impose periodic boundary condition on braided composite rve model based on rpim. *Composite Structures*, 163:77–88, 2017.

[105] T. Warburton and J.S. Hesthaven. On the constants in hp-finite element trace inverse inequalities. *Computer Methods in Applied Mechanics and Engineering*, 192(25):2765 – 2773, 2003.

[106] Barbara I Wohlmuth. Discretization techniques based on domain decomposition. *Discretization Methods and Iterative Solvers Based on Domain Decomposition*, pages 1–84, 2001.

[107] BI Wohlmuth, A Popp, MW Gee, and WA Wall. An abstract framework for a priori estimates for contact problems in 3d with quadratic finite elements. *Computational Mechanics*, 49(6):735–747, 2012.

[108] P Wriggers and Giorgio Zavarise. A formulation for frictionless contact problems using a weak form introduced by nitsche. *Computational Mechanics*, 41(3):407–420, 2008.

[109] Bin Yang and Tod A. Laursen. A contact searching algorithm including bounding volume trees applied to finite sliding mortar formulations. *Computational Mechanics*, 41(2):189–205, Jan 2008.

[110] LY Yao, DJ Yu, XY Cui, and XG Zang. Numerical treatment of acoustic problems with the smoothed finite element method. *Applied Acoustics*, 71(8):743–753, 2010.

[111] John Yen and Reza Langari. *Fuzzy logic: intelligence, control, and information*, volume 1. Prentice Hall Upper Saddle River, NJ, 1999.

[112] Zheng Yuan and Jacob Fish. Toward realization of computational homogenization in practice. *International Journal for Numerical Methods in Engineering*, 73(3):361–380, 2008.

[113] Paul A. Yushkevich, Joseph Piven, Heather Cody Hazlett, Rachel Gimpel Smith, Sean Ho, James C. Gee, and Guido Gerig. User-guided 3D active contour segmentation of anatomical structures: Significantly improved efficiency and reliability. *Neuroimage*, 31(3):1116–1128, 2006.

[114] X.-Y. Zhou, P.D. Gosling, C.J. Pearce, Z. Ullah, and L. Kaczmarczyk. Perturbation-based stochastic multi-scale computational homogenization method for woven textile composites. *International Journal of Solids and Structures*, 80:368 – 380, 2016.

[115] Olgierd Cecil Zienkiewicz, Robert Leroy Taylor, Olgierd Cecil Zienkiewicz, and Robert Lee Taylor. *The finite element method*, volume 36. McGraw-hill London, 1977.